Atomic Layer Deposition of Chalcogenide Materials for Large-Capacity and Low-Power Phase Change Memory

by

Chanyoung Yoo

August 2021

Department of Materials Science and Engineering

College of Engineering

Seoul National University

Atomic Layer Deposition of Chalcogenide Materials for Large-Capacity and Low-Power Phase Change Memory

Advisor: Prof. Cheol Seong Hwang

By

Chanyoung Yoo

A thesis submitted to the Graduate Faculty of Seoul National University in partial fulfillment of the requirements for the Degree of Doctor of Philosophy Department of Materials Science and Engineering

August 2021

Approved

by

Chairman of Advisory Committee:	<u>Sangbum Kim</u>
Vice-chairman of Advisory Committee:	<u>Cheol Seong Hwang</u>
Advisory Committee:	<u>Hyejin Jang</u>
Advisory Committee:	<u>Taeyong Eom</u>
Advisory Committee:	<u>Sijung Yoo</u>

Table of Contents

(1)   Yoo, S.; Yoo, C.; Park, E. S.; Kim, W.; Lee, Y. K.; Hwang, C. S. Chemical Interactions in the Atomic Layer Deposition of Ge-Sb-Se-Te Films and Their Ovonic Threshold Switching Behavior. *J. Mater. Chem. C* **2018**, 6 (18), 5025–5032.

(2)   Yoo, C.; Kim, W.; Jeon, J. W.; Park, E. S.; Ha, M.; Lee, Y. K.; Hwang, C. S. Atomic Layer Deposition of Ge_xSe_{1-x} Thin Films for Endurable Ovonic Threshold Selectors with a Low Threshold Voltage. *ACS Appl. Mater. Interfaces* **2020**, 12 (20), 23110–23118.

(3)   Yoo, C.; Atomic Layer Deposition of $GeTe/Sb_2Te_3$ Superlattice for Large-Capacity and Low-Power Phase Change Memory. Preparing for submission

List of Figures

List of Abbreviations

AES	Auger Electron Spectroscopy
AFM	Atomic Force Microscope
ALD	Atomic Layer Deposition
BL	Bit Line
CBA	Crossbar Array
CVD	Chemical Vapor Deposition
DC	Direct Current
DFT	Density Functional Theory
DRAM	Dynamic Random Access Memory
DUT	Device Under Test
EDS	Energy Dispersion Spectroscopy
FFT	Fast Fourier Transform
FIB	Focused Ion Beam
GAXRD	Grazing Angle incidence X-ray Diffraction
GST	Ge-Sb-Te alloys
GST225	$Ge_2Sb_2Te_5$ alloys
HAADF	High-Angle Annular Dark-Field
HRS	High Resistance State
HRTEM	High Resolution Transmission Electron Microscopy
IPCM	Interfacial Phase-Change Memory
I_{RESET}	RESET Current
I-V	Current-Voltage
J_{RESET}	RESET Current Density
LRS	Low Resistance State

MBE	Molecular Beam Epitaxy
OSC	Oscilloscope
OTS	Ovonic Threshold Switch
PCM	Phase-Change Memory
PG	Pulse Generator
PVD	Physical Vapor Deposition
RMS	Root Mean Square
SCCM	Standard Cubic Centimeter per Minute
SCM	Storage-Class Memory
SE	Spectroscopic Ellipsometry
SEM	Scanning Electron Microscope
SL	Superlattice
SSA	Solid-State Amorphization
STEM	Scanning Transmission Electron Microscopy
TEM	Transmission Electron Microscopy
V-CBA	Vertical-type Crossbar Array
vdW	van der Waals
V-PCM	Vertical-type Phase-Change Memory
VASP	Vienna *Ab-initio* Simulation Package
WL	World Line
XPS	X-ray Photoelectron Spectroscopy
XRD	X-ray Diffraction
XRF	X-ray Fluorescence
XRR	X-ray Reflectometry

1. Introduction

1.1. Overview and Issues on Phase-Change Memory

Global demand for data storage and processing has increased exponentially in recent decades with the development of information technologies such as mobile electronics, artificial intelligence, cloud computing, and supercomputing. International Data Corporation (IDC) reported that the amount of data consumed worldwide would reach 180 zettabytes in 2025, which surpasses the capabilities of the current computing architectures.[1] Research efforts have been dedicated to developing new emerging memories and neuro-inspired computing technologies and change the computing architectures to address limitations and meet the global demand. In particular, storage-class memory (SCM) was introduced to improve the bottleneck caused by the performance gap between fast, volatile dynamic random access memories (DRAM) and non-volatile but slow solid-state drives (SSD). SCM can simplify the current memory hierarchy and improve computing efficiency. Among several emerging memory candidates, phase-change memory (PCM) is the most mature product due to its high operating speed, excellent scalability, long data retention, and multi-level storage capabilities.[2,3] PCM was first introduced with the ovonic threshold switching (OTS) phenomenon measured

by Ovshinsky in the late 1960s.[4,5] After much research, Intel and Micron have brought PCM to the market as an SCM application in 2015 (called Optane).

PCM is based on chalcogenide material that undergoes a rapid and reversible phase transition.[6–9] The distinct contrast of electrical resistance between the amorphous (high resistance) and crystalline (low resistance) phase provides the ability to store and read data. Stored data are guaranteed to be non-volatile over ten years at room temperature with write times of just a few ten nanoseconds. The RESET process is performed by applying a large electrical pulse over a short period, allowing melting and subsequent quenching to amorphize a particular region. This amorphous region is connected in series with the remaining crystal regions and determines the PCM cell's high resistance state. The SET process can be achieved by applying a smaller but longer electrical pulse to recrystallize the local amorphous regions. The READ operation involves measuring the resistance by applying a low voltage pulse that does not interfere with the phase. The repeatability of the SET/RESET operations, usually over 10^8 cycles, is a significant advantage over the traditional non-volatile NAND flash memory, where the endurance is limited to 10^4–10^5. The SET process generally requires a longer time to crystallize the amorphous region, thus determining the PCM's operating speed. The RESET process determines the operating power due to the high current required to reach the melting temperature *via* Joule heating.

Chalcogenide materials are a group of VI-A elements that refer to sulfides, selenides, and tellurides.[4] The chalcogenides' unique lone pair characteristics enable the threshold switching in the amorphous phase, a dynamic 'ON state' in which resistance drops rapidly at a certain voltage.[10,11] Depending on the operation modes, the large current induced by this threshold switching can be volatile or crystallize the active region *via* Joule heating. The voltage pulse may be removed before the material crystallizes and reverts to the highly resistive amorphous phase. This volatile switch refers to the 'selector,' which is used to access a particular memory cell without misleading sneak currents.[12] On the other hand, applying a voltage pulse long enough to crystallize the material can switch the resistance with non-volatility, which is used as a memory cell. Among various chalcogenide material options for memory application, Ge-Sb-Te (GST) ternary compounds along the pseudobinary GeTe-Sb$_2$Te$_3$ tie line such as Ge$_1$Sb$_2$Te$_4$, Ge$_2$Sb$_2$Te$_5$, and Ge$_3$Sb$_2$Te$_6$ are the material of choice due to their fast and stable phase transition along with high resistance difference. Ternary compounds of this pseudobinary tie line have different behavior by changing the GeTe : Sb$_2$Te$_3$ composition. The higher ratio of GeTe to Sb$_2$Te$_3$ can increase stability and data retention, whereas the crystallization speed decreases instead. In particular, Ge$_2$Sb$_2$Te$_5$ (GST225) is the most widely used composition due to its proper compromise between the two tradeoffs.

Amorphization of the RESET process involves melting at high temperatures above T$_{melt}$ ~900K. A high RESET current is required to raise the temperature

3
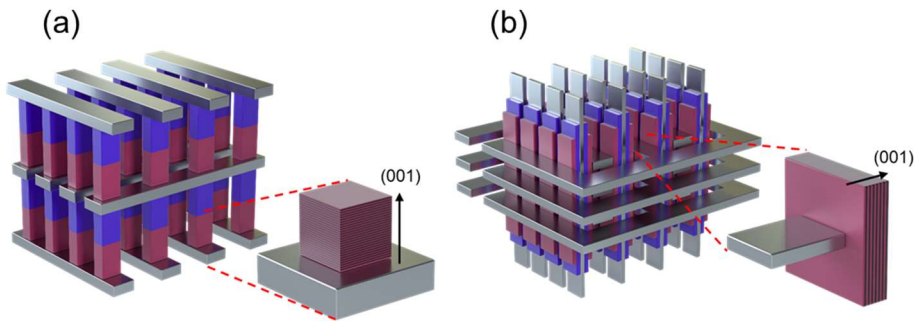
Figure 1-1. Schematic diagrams of an (a) planar-type and (b) vertical-type crossbar array structure. The insets show the GeTe/Sb$_2$Te$_3$ superlattice film orientation with van der Waals interlayers perpendicular to the metal electrode.

via Joule heating, which limits the step towards practical applications of the PCM. Scaling down the cell size can effectively lower the RESET current by reducing the switching volume. Still, selectors integrated in series with the memory cells are limited in scaling down to provide the high current required for RESET operation. Therefore, reducing RESET current is needed for the material or structural approach to achieve lower power and high-density memory. Tominaga *et al.*[13,14] suggested an alternative non-thermal switching using $GeTe/Sb_2Te_3$ superlattice material. The $GeTe/Sb_2Te_3$ superlattice, so-called the Interfacial Phase-Change Memory (IPCM), attracted intensive attention due to its low RESET current than the conventional Ge-Sb-Te alloys. The $GeTe/Sb_2Te_3$ superlattice's resistance change is known to be induced by local switching of the Ge atom between octahedral sites and lower-coordination sites at the interface of the superlattice layers.[14]

Meanwhile, the current PCM structure relies on the crossbar array (CBA) architecture, as shown in Figure 1-1 (a). The arrays have perpendicular access lines (bit lines (BL) and word lines (WL)), where a memory element resides at the intersection between each BL and WL. A stack of the planar arrays can form denser memory where the individual memory cell has a feature size of $4F^2/n$ (F: the feature size of a technology node, and *n*: the number of stacked layers). Since the commercial product (Optane) was first launched as a two-layered CBA in 2015, layers have not been increased yet. The CBA cannot keep up with the ultra-high density demands of low cost per bit due to the increased

fabrication cost by the lithography steps and masks required for each stacking layer. This significant problem is related to the fabrication of WL and BL per stack layer, which inevitably increases the peripheral area. It can be best addressed by the state-of-the-art vertical NAND (V-NAND) architecture as in Figure 1-1 (b), proven technology with a stack of more than 150 layers. The V-NAND architecture provides the most efficient way to add memory layers for ultra-high density with extremely low yield loss since the fabrication requires far fewer lithography steps and masks. To fabricate highly integrated V-NAND architecture memory, the process starts from alternately depositing dielectric (e.g., SiO_2) and metal (e.g., TiN) layers (this determines the total number of stacks) and involves the etching process for deep holes to expose the electrodes. The phase-change layer should be uniformly deposited on the inner surface of the deep etched holes in this vertical architecture, which could be accomplished only by the atomic layer deposition (ALD) method.[15]

The $GeTe/Sb_2Te_3$ superlattice deposition on the etched sidewall is more challenging than the Ge-Sb-Te alloy case. The $GeTe/Sb_2Te_3$ superlattice exhibits low electrical characteristics only when its van der Waals (vdW) interlayers are aligned perpendicular to the metal electrode (the direction in which the voltage is applied). In the V-NAND architecture, the $GeTe/Sb_2Te_3$ must be aligned on the sidewall in the same way as the planar-type structure to have its high performance (as in the inset figures in Figure 1-1). This is a process that is not feasible with any other deposition methods. Only ALD

makes this possible through a self-limiting chemical reaction between the precursors and the structured substrate with isotropic directions.

1.2. Objective and Chapter Overview

The objective of the present thesis is focused on the ALD of chalcogenide materials, including $GeTe/Sb_2Te_3$ superlattice and amorphous Ge_xSe_{1-x} films. The ALD process demonstrates the feasibility of vertical crossbar arrays for ultra-dense and low-power phase-change memory.

Chapter 2 describes the ALD of $GeTe/Sb_2Te_3$ superlattice film for large-capacity and low-power phase-change memory. Synthesis of the superlattice by a cyclic modification of ALD and film alignment for planar/vertical-type device fabrication is performed. The in-depth structural analysis and the switching mechanism of low I_{RESET} are also covered.

Chapter 3 covers the deposition process of amorphous Ge_xSe_{1-x} film using $Ge(N(Si(CH_3)_3)_2)_2$ and $((CH_3)_3Si)_2Se$ as Ge- and Se- precursors. The unique deposition mechanism that involves Ge intermediates provided a way to modulate the film composition. The film properties and high conformal growth are examined, and the ovonic threshold switch characteristics of the Ge_xSe_{1-x} film at each composition are also performed.

Finally, in chapter 4, the conclusion of the thesis is made.

1.3. References

(1)   Wang, Z.; Wu, H.; Burr, G. W.; Hwang, C. S.; Wang, K. L.; Xia, Q.; Yang, J. J. Resistive Switching Materials for Information Processing. *Nat. Rev. Mater.* **2020**, *5* (3), 173–195.

(2)   Fong, S. W.; Neumann, C. M.; Wong, H.-S. P. Phase-Change Memory— Towards a Storage-Class Memory. *IEEE Trans. Electron Devices* **2017**, *64* (11), 4374–4385.

(3)   Kim, T.; Lee, S. Evolution of Phase-Change Memory for the Storage-Class Memory and Beyond. *IEEE Trans. Electron Devices* **2020**, *67* (4), 1394–1406.

(4)   Ovshinsky, S. R. Reversible Electrical Switching Phenomena in Disordered Structures. *Phys. Rev. Lett.* **1968**, *21* (20), 1450–1453.

(5)   Ovshinsky, S. R. Localized States in the Gap of Amorphous Semiconductors. *Phys. Rev. Lett.* **1976**, *36* (24), 1469.

(6)   Burr, G. W.; Breitwisch, M. J.; Franceschini, M.; Garetto, D.; Gopalakrishnan, K.; Jackson, B.; Kurdi, B.; Lam, C.; Lastras, L. A.; Padilla, A.; Rajendran, B.; Raous, S.; Shenoy R. S. Phase Change Memory Technology. *J. Vac. Sci. Technol. B.* **2010**, 28 (2) 223.

(7)   Burr, G. W.; BrightSky, M. J.; Sebastian, A.; Cheng, H.-Y.; Wu, J.-Y.; Kim, S.; Sosa, N. E.; Papandreou, N.; Lung, H.-L.; Pozidis, H.; Eleftheriou, E.; Lam, C. H. Recent Progress in Phase-Change Memory Technology. *IEEE J. Emerg. Sel. Top. Circuits Syst.* **2016**, *6* (2), 1–17.

(8)   Lacaita, A. L.; Wouters, D. J. Phase-Change Memories. *Phys. Status Solidi Appl. Mater. Sci.* **2008**, *205* (10), 2281–2297.

(9)   Sarwat, S. G. Materials Science and Engineering of Phase Change Random

Access Memory. *Mater. Sci. Technol. (United Kingdom)* **2017**, *33* (16), 1890–1906.

(10)   Ielmini, D.; Zhang, Y. Analytical Model for Subthreshold Conduction and Threshold Switching in Chalcogenide-Based Memory Devices. *J. Appl. Phys.* **2007**, *102* (5).

(11)   Ielmini, D. Threshold Switching Mechanism by High-Field Energy Gain in the Hopping Transport of Chalcogenide Glasses. *Phys. Rev. B - Condens. Matter Mater. Phys.* **2008**, *78* (3), 1–8.

(12)   Burr, G. W.; Shenoy, R. S.; Virwani, K.; Narayanan, P.; Padilla, A.; Kurdi, B.; Hwang, H. Access Devices for 3D Crosspoint Memory. *J. Vac. Sci. Technol., B: Nanotechnol. Microelectron.: Mater., Process., Meas., Phenom.* **2014**, 32, No. 040802.

(13)   Tominaga, J. The Design and Application on Interfacial Phase-Change Memory. *Phys. Status Solidi - Rapid Res. Lett.* **2019**, *13* (4), 1–11.

(14)   Simpson, R. E.; Fons, P.; Kolobov, A. V.; Fukaya, T.; Krbal, M.; Yagi, T.; Tominaga, J. Interfacial Phase-Change Memory. *Nat. Nanotechnol.* **2011**, *6* (8), 501–505.

(15)   Lee, Y. K.; Yoo, C.; Kim, W.; Jeon, J. W.; Hwang, C. S. Atomic Layer Deposition of Chalcogenides for Next-Generation Phase Change Memory. *J. Mater. Chem. C* **2021**, *9* (11), 3708–3725.

2. Atomic Layer Deposition of GeTe/Sb$_2$Te$_3$ Superlattice for Large-Capacity and Low-Power Phase Change Memory

2.1. Introduction

Synthesizing non-natural materials, such as superlattice (SL), can provide functional properties that can hardly be achieved from the conventional alloy material. One example of such performance could be found from the superb resistance switching of GeTe/Sb$_2$Te$_3$ SL compared with the homogeneously mixed Ge-Sb-Te alloy with similar chemical composition.[1–5] The Ge-Sb-Te (GST) ternary compounds along the pseudobinary GeTe-Sb$_2$Te$_3$ tie line, especially Ge$_1$Sb$_2$Te$_4$ (GST124) and Ge$_2$Sb$_2$Te$_5$ (GST225), have been extensively studied among the various chalcogenide-based phase-change materials, which are the core element of the phase-change memory (PCM).[6–9] Nonetheless, its thermal melting and subsequent quenching mechanism for the amorphization brings several problems, such as high RESET current (I_{RESET}), material degradation by local compositional segregation, and thermal interference between the neighboring memory cells.

The sputtered GeTe/Sb$_2$Te$_3$ SL, called the interfacial phase-change memory (IPCM), was suggested as an alternative contender to solve such

problems.[1] The IPCM is composed of alternately stacked GeTe and Sb_2Te_3 layers with the van der Waals (vdW) gaps aligned parallel to the substrate, contrasting with the homogeneous and randomly oriented GST alloys. In IPCM, it was argued that the electrical resistance switching is mediated by the local switching of Ge atoms at the interface between the GeTe and Sb_2Te_3 layers, which was later identified as a kind of topological phase-change.[1] The IPCM required only ~half of the I_{RESET} of the homogeneous GST225 alloy material, which also showed additional merits of maintaining the structural integrity after the extensively repeated switching operations. Subsequent work by the molecular beam epitaxy (MBE) corroborated the original performance of the IPCM.[3,10–12]

Nonetheless, the precise mechanism of the improved switching performance, i.e., reduction of I_{RESET}, is still controversial. Tominaga et al.[1] claimed that the SL structure creates a material in which Ge atoms can switch between octahedral sites and lower-coordination sites at the interface of the SL layers. More specifically, the atomic arrangement of the GeTe layer at the SL interfaces changes between Ferro (low resistance state) and inverted-Petrov (high resistance state). Low current switching is achieved by reducing the entropic losses attributed to a solid-state transition, which differs from the liquid phase transition that occurs typically in melt-quenched amorphous PCM. In contrast, Calarco et al.[3] reported that the GeTe/Sb_2Te_3 SL is actually composed of Sb_2Te_3 and GST layers. The GST layers cannot form a Ferro or

inverted-Petrov structure; instead, they form a Kooi structure where the Ge atoms are in the middle of the layer. They claimed that such Kooi structure could not accompany the collective Ge switching, and the switching mechanism is still a conventional melt-quench transition. In addition, several reports described the switching mechanism by enhanced thermal efficiency, stacking fault assisted transition, strain assisted transition, and partial amorphization. However, a comprehensive and integrated understanding of the switching mechanism is still lacking. This work provides unequivocal evidence that the $GeTe/Sb_2Te_3$ SL has a conventional amorphous–crystalline phase transition but proceeds by a pressure-induced solid-state amorphous (SSA) transition, which does not involve a melt-quenching process.

Meanwhile, the current PCM relies on the crossbar array (CBA) structure due to its condensed and straightforward architecture. However, the CBA cannot keep up with the ultra-high density demands due to the increased fabrication cost upon stacking. This can be best addressed by the state-of-the-art vertical NAND architecture,[13,14] proven technology with a stack of more than 150 layers. The V-NAND architecture provides the most efficient way to add memory layers for ultra-high density with extremely low yield loss since the manufacturing requires fewer lithography steps and masks. To fabricate highly integrated V-NAND architecture PCM, the phase-change layer should be uniformly deposited on the inner surface of the deep etched holes in this vertical architecture, which could be accomplished only by atomic layer

deposition (ALD). The peculiar chemical affinity of the Ge, Sb, and Te precursors to the substrate surface and the two-dimensional nature of the Sb_2Te_3 allowed the authors to adopt the ALD process to achieve the *in-situ* crystalized $GeTe/Sb_2Te_3$ SL. The ALD $GeTe/Sb_2Te_3$ SL significantly lowered the RESET current of randomly oriented GST225 alloy material grown by the identical ALD process, both for planar and vertical-type devices. This is a step-forward improvement in the PCM field for the mushroom-type conventional PCM and the futuristic V-PCM.

2.2. Experimental

The film deposition was performed using a shower-head-type ALD reactor with an 8-inch wafer-scale (CN-1, Puls-200). $Ge^{II}NMe_2[(NiPr)_2CNMe_2]$, $Sb(OC_2H_5)_3$, and $((CH_3)_3Si)_2Te$ were used as the Ge, Sb, and Te precursors, respectively. The precursors were carried into the ALD reactor with 50 standard cubic centimeters per minute (sccm) of Ar carrier gas, while 50 sccm NH_3 gas was co-injected with Te precursor. SiO_2/Si (100 nm thick) and TiN/SiO_2/Si (50 nm thick) were used as substrates, where SiO_2 and TiN films were prepared by dry oxidation and sputtering (Applied Materials, Endura 5500), respectively.

The crystallinity and crystal orientation were measured using both θ-2θ and glancing X-ray diffraction (XRD, PANalytical, X'Pert PRO MPD). X-ray photoelectron spectroscopy (XPS, Kratos, AXIS SUPRA) was performed to confirm the element's chemical states of the Sb_2Te_3 film. Cross-sectional TEM and EDS images were performed with a Cs-corrected transmission electron microscopy (Cs-TEM, JEOL, JEM-ARM200F) using specimens prepared with a focused ion beam (FBI, Thermo Fisher Scientific, Helios G4). Scanning electron microscopy (SEM, Hitachi, S-4800) was used for imaging the film surface.

Ab-initio calculations were performed using the Vienna *Ab-initio* Simulation Package (VASP). Grimme's D2 correction (DFT+D2) was

employed to describe vdW interaction with the Perdew-Burke-Ernzerhof (PBE) functional. *Ab-initio* molecular dynamic (MD) calculations were performed to describe amorphous SiO_2 and the interface structure with Sb_2Te_3 and amorphous SiO_2.

2.3. Results and Discussions

2. 3. 1. Synthesis of the GeTe/Sb₂Te₃ Superlattice

The authors previously reported the NH_3 co-reactant mediated chemistry-specific ALD process of growing the GeTe and Sb_2Te_3 layers at substrate temperatures of 130 – 170 ºC, where the Ge-, Sb-, and Te-precursors are $Ge^{II}NMe_2[(NiPr)_2CNMe_2]$, $Sb(OC_2H_5)_3$, and $((CH_3)_3Si)_2Te$, respectively.[15,16] When the NH_3 gas was co-injected with the $((CH_3)_3Si)_2Te$, the gas-phase intermediate reaction species, H_2Te, were formed. The formation of H_2Te intermediate induced facile ALD *via* the ligand-exchange reaction with the adsorbed Ge-, and Sb-precursors. The high-quality GST alloy film with various GeTe to Sb_2Te_3 ratios could be grown by combining the GeTe and Sb_2Te_3 ALD subcycles to form a supercycle. However, the previous works did not attempt the growth of the uniformly oriented GeTe and Sb_2Te_3 layers.[17] Here, the growth of GeTe/Sb_2Te_3 SL where the GeTe and Sb_2Te_3 layers are uniformly oriented along the substrate with a particular orientation is attempted. Figure 2-1 summarizes the overall deposition process and chemical reactions for the ALD GeTe/Sb_2Te_3 SL. The GeTe/Sb_2Te_3 SL films were deposited through a rather complicated process, in which the pre-treatment of the substrate surface for the film alignment was performed at a substrate temperature of 130 ºC, followed by the deposition of Sb_2Te_3 and GeTe films alternately in 40 and 10 cycles, respectively, at an elevated temperature of
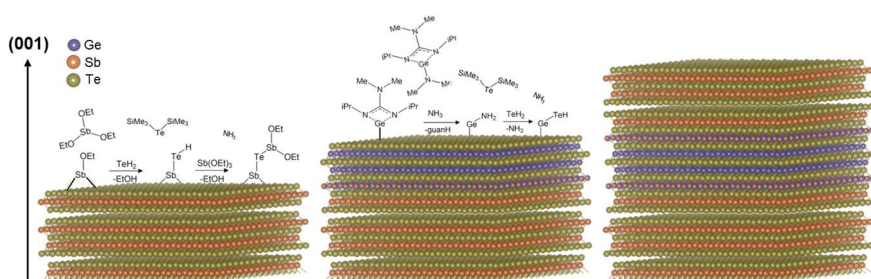
Figure 2-1. Schematic diagram and chemical reactions of the Ge, Sb, and Te precursors for the ALD GeTe/Sb$_2$Te$_3$ film deposition process
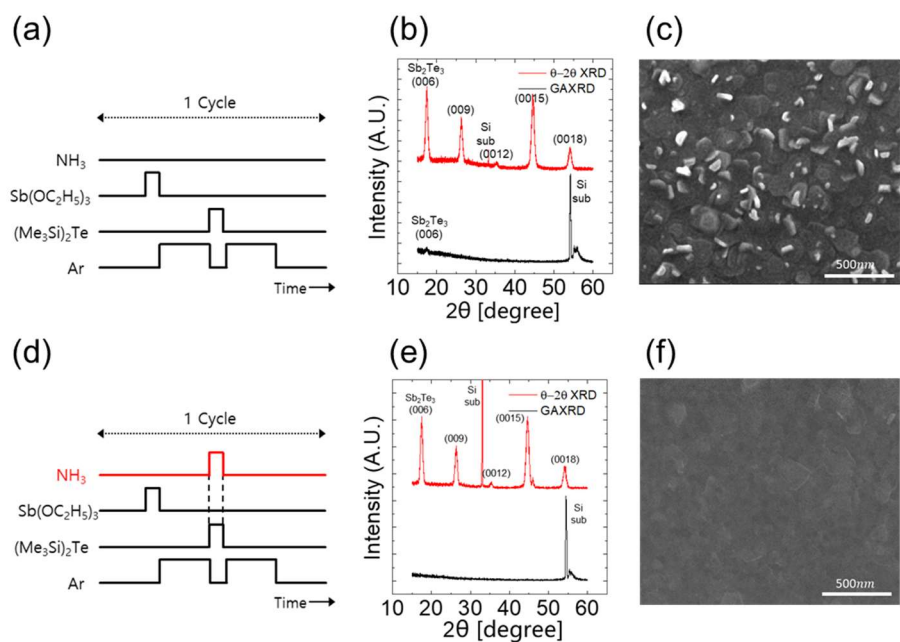
Figure 2-2. The ALD sequence, XRD, and top-view SEM images of the Sb_2Te_3 film on SiO_2 substrate (a)-(c) without and (d)-(f) with NH_3 co-injection

170 °C. The role of each processes will be explained in detail.

The first critical step in this work was to grow a fully c-axis-oriented Sb_2Te_3 film on a SiO_2 substrate surface.[18–20] This could be ascribed to the layered structure of the Sb_2Te_3 material, where the two Sb layers were intervened between the three Te layers (see the left panel of Figure 2-1). The layer-by-layer growth with its c-axis-alignment completely on SiO_2 substrate was only accomplished with the NH_3 co-injection as in Figure 2-2. A typical ALD process without the NH_3 co-injection deposited low-quality Sb_2Te_3 films with randomly oriented grains (Figures 2-2 (a)–(c)). However, with the modification of the ALD sequence to 'Sb precursor injection – Ar purge – Te precursor co-injected with NH_3 – Ar purge' accordingly, the Sb_2Te_3 film had highly preferred c-axis crystal orientation with the vdW interlayers parallel to the substrate (Figures 2-2 (d)–(f)). No diffraction peaks were observed in the GAXRD with the modified NH_3 co-injection sequence, but only the (00l) plane peaks appeared in the out-of-plane θ-2θ XRD (Figure 2-2 (e)). The top-view SEM images in Figures 2-2 (c) and (f) also support the alignment effect of the NH_3 co-injection. The Sb_2Te_3 plates were tilted and protruded without NH_3 co-injection, whereas smooth surfaces with aligned plates appeared with NH_3 co-injection. It should be noted that the c-axis-aligned Sb_2Te_3 films are not single crystalline but polycrystalline with random in-plane grain orientations.
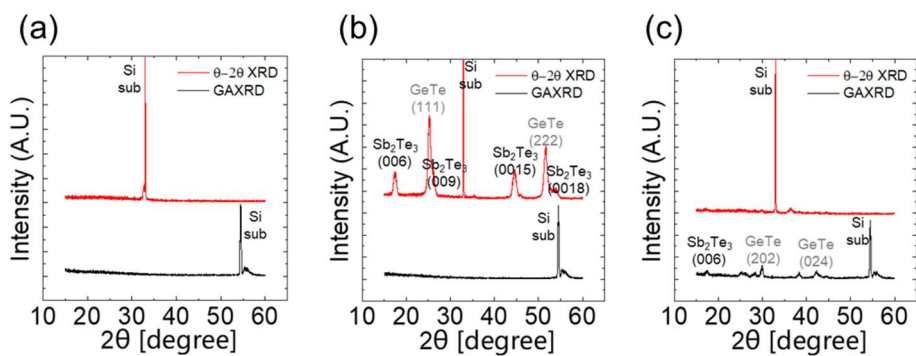
Figure 2-3. XRD diffraction patterns of the GeTe film (a) on SiO_2 substrate, (b)

on c-axis oriented Sb_2Te_3, and (c) on non-oriented Sb_2Te_3
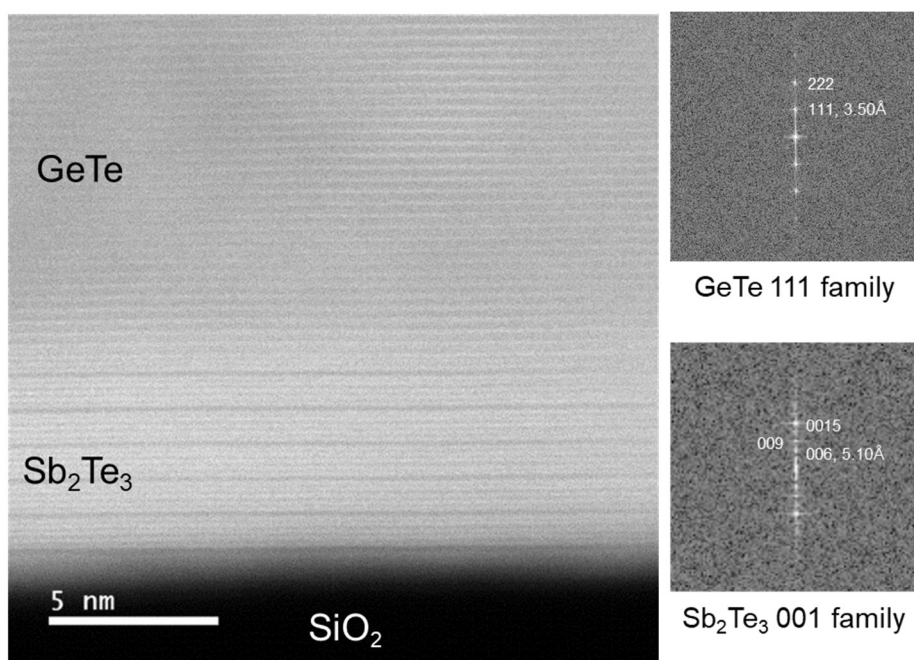
Figure 2-4. Cross-sectional STEM image of highly oriented Sb_2Te_3 and GeTe

layer deposited on SiO_2 substrate. The right inset shows the FFT

of each layer

Once the fully c-axis-aligned Sb_2Te_3 layer was grown, further growth of 111-oriented GeTe layer growth on top of the Sb_2Te_3 seed layer was feasible due to the negligible lattice mismatch between the (001) plane of Sb_2Te_3 and (111) plane of GeTe (Sb_2Te_3: a=4.26Å, $R\bar{3}m$; GeTe: a_{111}=4.25Å, $Fm\bar{3}m$). Figure 2-3 (b) shows the XRD patterns of the GeTe layer deposited on a well-aligned Sb_2Te_3 film. Only the (111) and (222) peaks of the $Fm\bar{3}m$ GeTe were observed in the θ-2θ XRD without any GAXRD peaks. Figure 2-4 shows the cross-sectional scanning transmission electron microscopy (STEM) image and the fast Fourier transform (FFT) of GeTe/Sb_2Te_3 bilayer film composed of a 6 nm thick Sb_2Te_3 / 20 nm thick GeTe film on the SiO_2 substrate. The layer-by-layer arrangement of the two portions of the film could be clearly identified, suggesting that the 111-direction alignment of the GeTe layer could be retained up to a quite thick thickness (20 nm). The attempt to directly grow the GeTe film on a SiO_2 substrate resulted in an amorphous structure at a substrate temperature of 170 °C, as confirmed by the absence of diffraction peaks in the θ-2θ and GAXRD diffraction patterns shown in Figure 2-3 (a). This suggests that the lattice matching effect surely induces an *in-situ* crystallization of the GeTe film with the underlying crystallized Sb_2Te_3.[21] Of note, the GeTe film deposited on non-oriented Sb_2Te_3 film did not show the preferred orientation (Figure 2-3 (c)).

Based on this finding, the GeTe/Sb_2Te_3 SL fabrication was attempted. The desired thicknesses of the Sb_2Te_3 and GeTe layers were 4 and 1 nm thick,
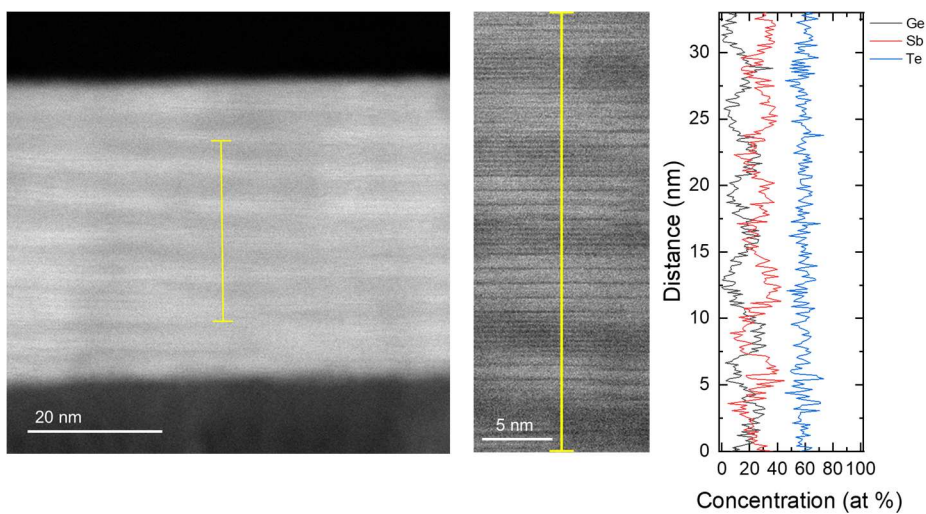
Figure 2-5. Cross-sectional STEM (left), TEM (middle), and EDS (right) image of the GeTe/Sb$_2$Te$_3$ superlattice film. The Ge, Sb, and Te concentration line profile is obtained from the yellow line region marked in the TEM images.
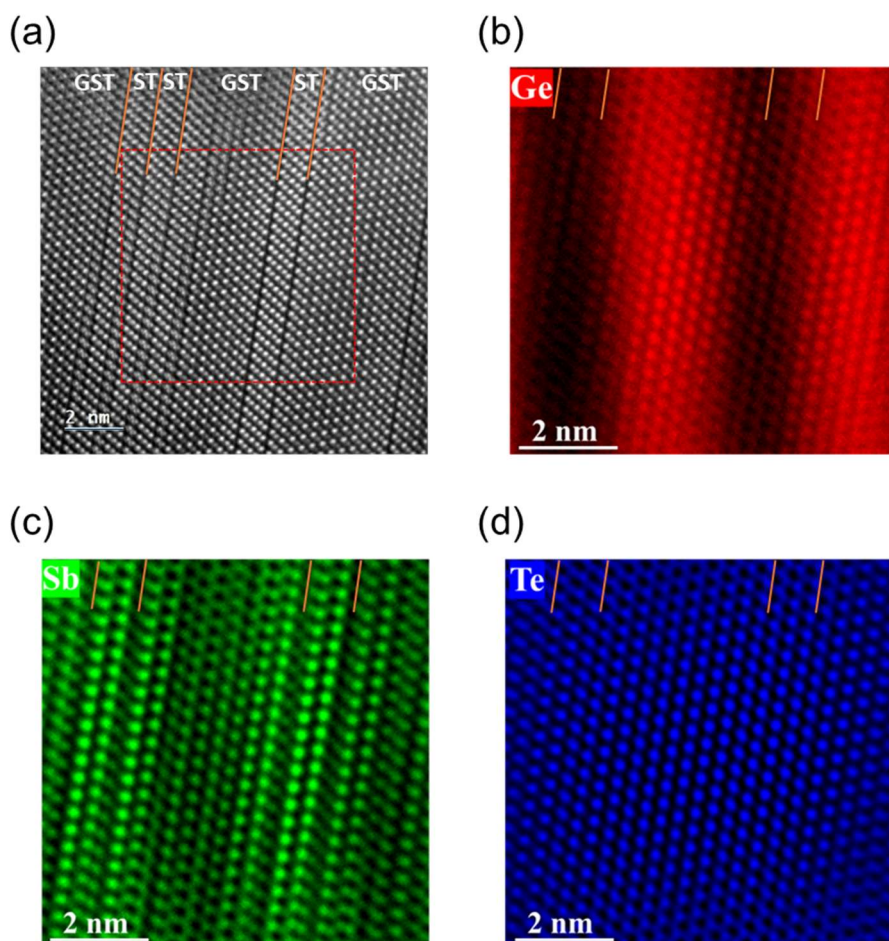
Figure 2-6. (a) HAADF-STEM pattern of the ALD GeTe/Sb_2Te_3 superlattice and the EDS mapping of (b) Ge, (c) Sb, and (d) Te atoms of the local phase indicated by the red box. The orange lines indicate vdW gaps.

respectively, which was adapted from the IPCM work of Prof. Tominaga's group.[1,2] To achieve these thicknesses, 40 and 10 cycles of the Sb_2Te_3 and GeTe ALD were performed, and such ALD supercycle was repeated eight times in total. Figure 2-5 shows a cross-sectional STEM image of the SL film repeated eight times with a 1.5/3.5 nm thick $GeTe/Sb_2Te_3$. The right portion of the figure shows the high-resolution image (the brighter portions with dark horizontal lines correspond to the Sb_2Te_3 regions while the thicker grey regions correspond to the GeTe regions) and the corresponding energy dispersive spectroscopy (EDS) line scan result. It can be understood that the two layers form an SL structure, while the slight intermixing at the interface cannot be excluded.[22]

Figure 2-6 shows the STEM-high angle annular dark-field (HAADF) image of the ALD $GeTe/Sb_2Te_3$ SL and the EDS mapping of each atom. As in Figure 2-6 (a), the $GeTe/Sb_2Te_3$ SL structure is comprised of 5 and 19 atomic layers. The blocks with five atomic layers are Sb_2Te_3 quintuple, and the 19 atomic layers are intermixed GST. This indicates that the $GeTe/Sb_2Te_3$ SL film is not an SL of GeTe and Sb_2Te_3 but is actually composed of GST and Sb_2Te_3 layers where the Ge atomic preferentially present at the center portion of the GST layers.[11] The intermixing of the GeTe and Sb_2Te_3 layer is energetically favorable because it increases the configurational entropy and releases strain by reducing the mismatch between GeTe and Sb_2Te_3 layers. The EDS mapping in Figures 2-6 (b)–(d) reveals that the Sb-rich planes locate adjacent to the vdW

26
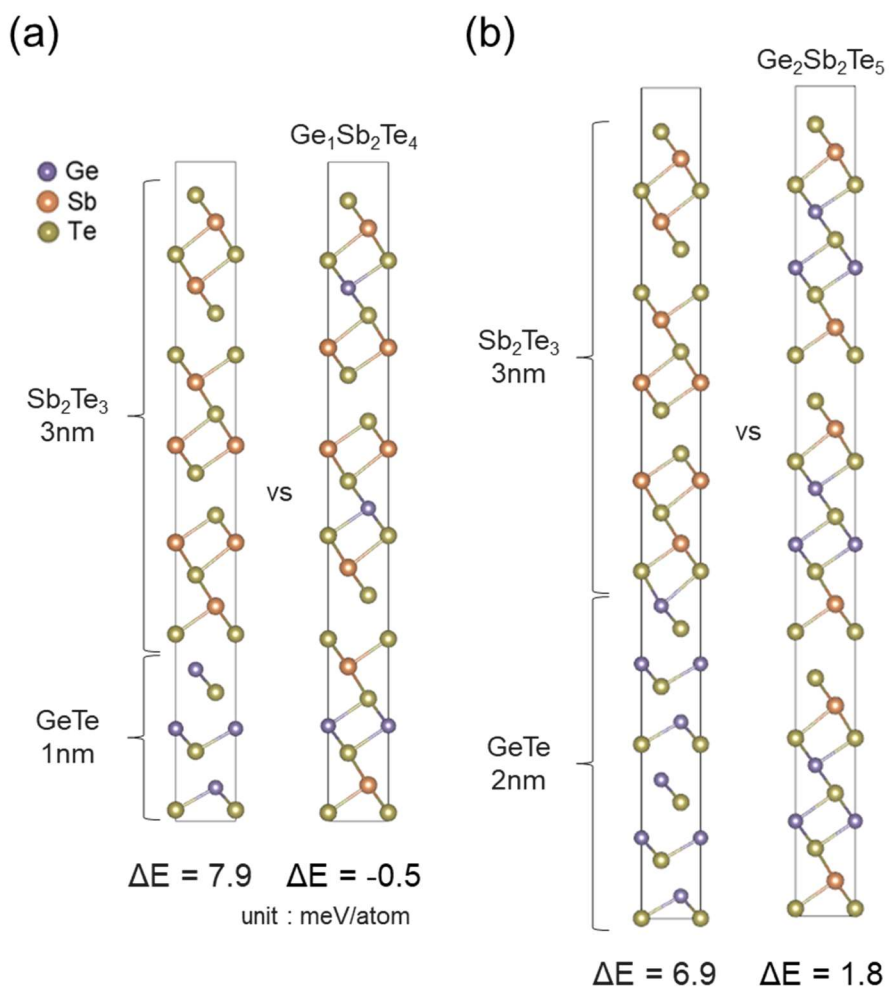
Figure 2-7. Formation energy of GeTe/Sb$_2$Te$_3$ and intermixed (a) Ge$_1$Sb$_2$Te$_4$ and (b) Ge$_2$Sb$_2$Te$_5$ alloy.

gaps (the orange lines indicate the vdW gaps and confirm that the Sb atoms are near the orange lines). Ge-rich planes locate more distant from the vdW gaps of the 19 layered blocks, which can be considered a Kooi structure.[23,24] The first principle simulation verified the energetically favorable intermixing of GeTe/Sb_2Te_3 and the formation of the GST Kooi structure. The formation energy of the strained GeTe/Sb_2Te_3 and intermixed GST alloys were calculated and compared in Figures 2-7. As expected, the Kooi structure intermixed with GeTe and Sb_2Te_3 layers were energetically favorable over having a separated structure with strains. Such intermixed Kooi GST and ST structures cannot accompany the local switching of Ge proposed by Prof. Tominaga's group, in which the Ge atoms switch between Ferro (low resistance state) and inverted-Petrov (high resistance state).[2] Details of the switching mechanism are described in section 2.3.3.

2. 3. 2. Film Alignment and Device Fabrication

Although the successful ALD of GeTe/Sb$_2$Te$_3$ film on SiO$_2$ substrate was a significant first step toward the IPCM fabrication, such an SL growth must also be confirmed on a polycrystalline TiN surface (or W surface) for electrical measurements. However, only randomly oriented films were achieved when the identical SL growth process with NH$_3$ co-injection was attempted on a reactively sputtered TiN substrate, either as-grown or chemical mechanically polished (also on the W film surface). The inhomogeneous film surface morphology of the Sb$_2$Te$_3$ film grown on TiN substrate, observed by the SEM, can be found in Figure 2-8 (a). The diffraction peaks of the (015) and (100) planes in GAXRD and the negligible (00l) plane peaks in θ-2θ XRD pattern in Figure 2-8 (b) provided the additional crystallographic proof for the non-alignment of the Sb$_2$Te$_3$ film on the TiN substrates. If the film is fully c-axis-aligned, diffraction peaks must be seen only in θ-2θ XRD but not in the GAXRD, which was the case on SiO$_2$ substrate (Figures 2-2 (d)–(f)).

To achieve c-axis-aligned Sb$_2$Te$_3$ layer both on SiO$_2$ and TiN substrates simultaneously, the chemical interactions between the Sb-and Te-precursors with the two types of substrate surfaces were examined in the following way. The two samples with the SiO$_2$ and TiN substrates were simultaneously loaded into the ALD chamber and heated to 130 °C. Then, either Sb- or Te-precursor was pulsed 100 cycles with the NH$_3$ co-injection (2 s pulse - 15 s Ar purge).
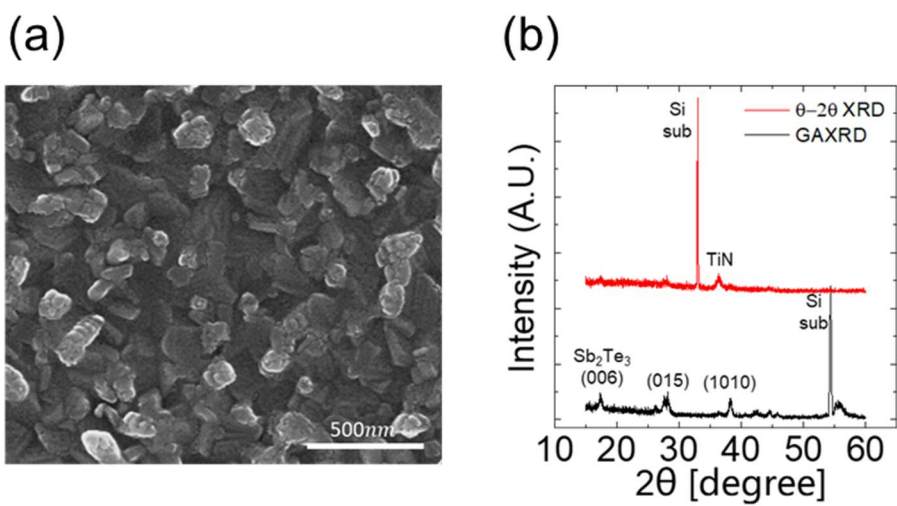
Figure 2-8. (a) Top-view SEM image and (b) XRD patterns of the ALD Sb_2Te_3

film deposited on TiN substrate
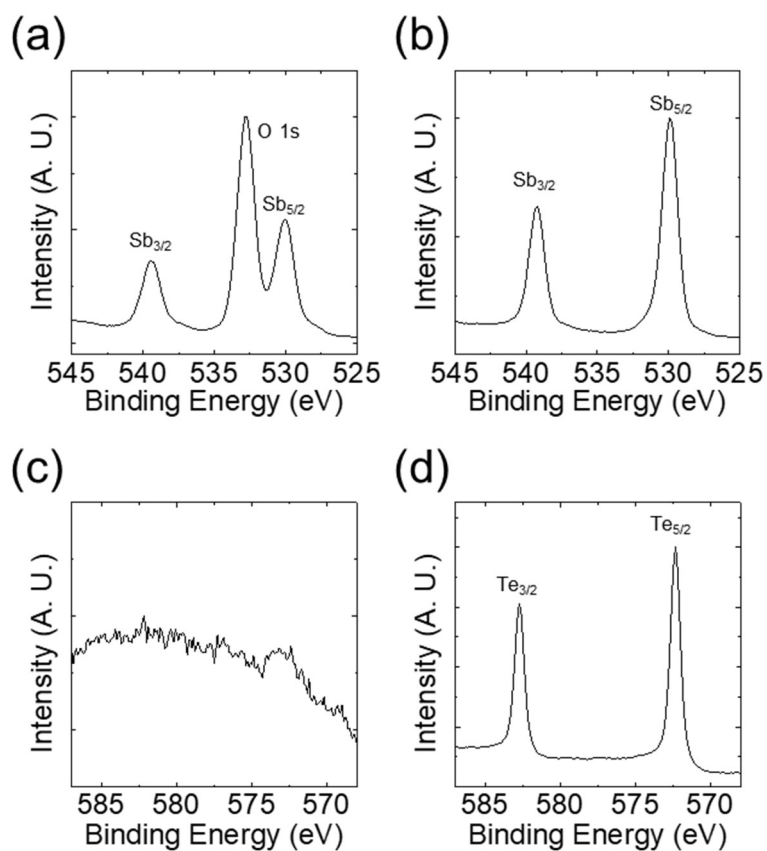
Figure 2-9. XPS spectra of (a)-(b) Sb $3d$ and (c)-(d) Te $3d$ at the surface after

100 cycles of (a) Sb-only on SiO_2, (b) Sb-only on TiN, (c) Te-only

on SiO_2, and (d) Te-only on TiN
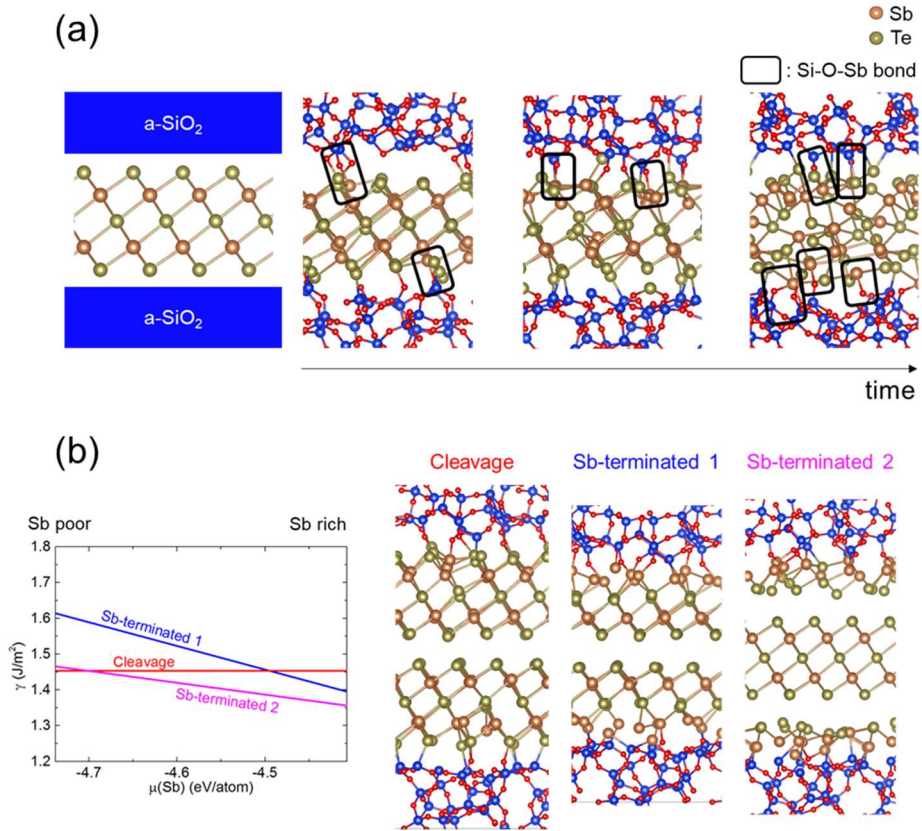
Figure 2-10. *Ab-initio* study of preferential interaction of Sb and Te with SiO_2 substrate. (a) *Ab-initio* calculation showing the evolution of the atomic structures of a single Sb_2Te_3 on amorphous SiO_2. (b) Interface energy of cleavage, and Sb-terminated structure**.**

The purpose of this experiment was to see if any of the two precursors can chemically adsorb on the two surfaces without the complete ALD cycles. Figures 2-9 (a) and (b) show the X-ray photoelectron spectroscopy (XPS) data of the Sb-treated SiO_2 and TiN surfaces, respectively. Both figures show Sb $3d$ peaks suggesting that the Sb-precursor can be chemically adsorbed on both surfaces. In contrast, Figures 2-9 (c) and (d) show the Te 3d XPS data of the Te-treated SiO_2 and TiN surfaces, demonstrating that the Te-precursor cannot be chemically adsorbed on the SiO_2 but can be on the TiN surface. This finding implies that the Sb_2Te_3 layer's growth on the SiO_2 surface, shown in Figure 2-2, was mediated by the first Sb-layer formation, which then triggers the adsorption of Te-precursors. This naturally induced the first growth of the Sb-layer, being followed by the Te-layer. Then, the identical layer-by-layer growth follows during the subsequent ALD process. Once the five-layer structure of the one whole Sb_2Te_3 crystal unit cell is completed, the next step is to start from the Te-layer, forming the bulk Sb_2Te_3 thin film's layered structure, which is governed by the Sb_2Te_3 material property.

The first principle simulation could further back up the formation of such a configuration for the $SiO_2/Sb_2Te_3/SiO_2$ sandwiched structure in Figure 2-10. The simulation trajectories show that the Sb element penetrates the termination Te layer and forms a robust Sb-O binding with the amorphous SiO_2 as in Figure 2-10 (a). Eventually, the quintuple layer of Sb_2Te_3 breaks, which will hinder the continuous aligned growth of the upper films. The Sb-terminated structure
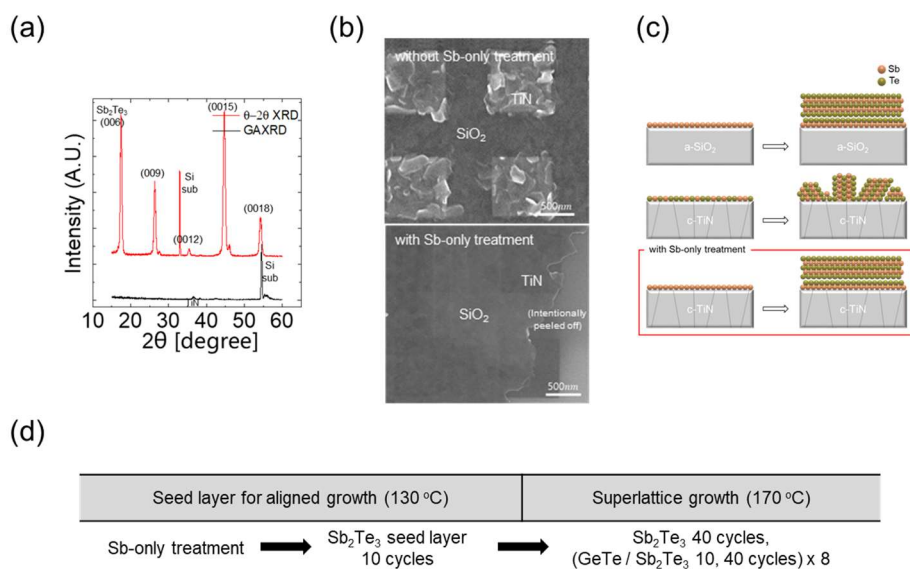
Figure 2-11. Process for alignment of the ALD GeTe/Sb$_2$Te$_3$ superlattice. (a) XRD patterns of the aligned Sb$_2$Te$_3$ film on TiN substrate by the Sb-only treatment. (b) Top-view SEM images of the Sb$_2$Te$_3$ film deposited without (top) and with (bottom) Sb-precursor-only treatment on a structure with 800x800 nm^2 TiN plugs repeated on SiO$_2$. (c) Schematic diagram of the Sb$_2$Te$_3$ film alignment. (d) The overall deposition process, including the number of cycles and substrate temperatures for each process.

was conceived to avoid unwanted structural modification, and its influence on structural stability was checked. In Figure 2-10 (b), the interface energies of the Sb_2Te_3/a-SiO_2 having two different Sb-termination types were calculated and compared with the cleavage case. The cleavage case has Sb_2Te_3 layers with Te atoms terminated on amorphous SiO_2, while the Sb-terminated structures have Sb atoms terminated. The Sb-terminated Sb_2Te_3/a-SiO_2 showed a more stable structure with lower interface energy than the cleavage Sb_2Te_3/a-SiO_2, and the case Sb-terminated 2 was found to have the lowest interfacial energy. Therefore, to deposit a well-aligned Sb_2Te_3 film, the element closest to the substrate should be Sb.

Such findings provide the authors with a clue to grow a fully c-axis-aligned Sb_2Te_3 film and subsequent 111-oriented GeTe on a TiN substrate, too. Instead of starting the growth process using the alternative injection of Sb- and Te-precursors, the TiN surface was pulsed with NH_3/Sb-precursor step 100 cycles at 130 °C, which must form a monolayer of Sb (or half ALD cycle completed Sb-precursors). Then, the usual Sb_2Te_3 ALD cycles were performed. Figure 2-11 (a) shows the θ-2θ and GAXRD data of the Sb_2Te_3 film grown by the Sb-only treatment and the subsequent normal Sb_2Te_3 ALD cycles (total thickness of 20 nm). The GAXRD shows diffraction peaks from only the TiN film and Si substrate, whereas the θ-2θ XRD shows peaks from the (00l) Sb_2Te_3 planes only. This suggests that the Sb_2Te_3 film is completely c-axis-aligned even on the TiN substrate. Figure 2-11 (b) shows the SEM image of the Sb_2Te_3
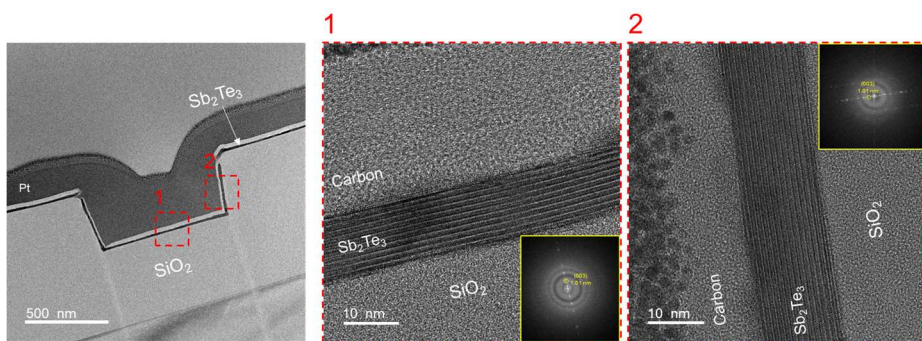
Figure 2-12. Cross-sectional TEM images of the ALD Sb_2Te_3 film on a trench pattern. The figures with a red border on the right are higher-magnified images of the local phases indicated by the red box and numbers on the left figure. The inset figures indicate the FFT result of the Sb_2Te_3 (003) plane.

film grown on the TiN plug wafer (square area with one edge length of 800 nm in the chemical vapor deposited 50 nm thick SiO_2 films) without (upper image) and with (lower image) the Sb-only treatment step. The upper image reveals that the Sb_2Te_3 film on the TiN portion includes randomly oriented Sb_2Te_3 grains, whereas uniformly aligned microstructures are formed on the SiO_2 portion, of which the out-of-plane direction must be the c-axis direction. In contrast, the lower image shows that the entire wafer surface is covered with the homogeneously c-axis-aligned Sb_2Te_3 grains, demonstrating the feasible accomplishment of the goal. Figure 2-11 (c) schematically summarizes the different Sb_2Te_3 layer growth behaviors on the SiO_2 and TiN substrates depending on the Sb-only treatment steps. On this c-axis-aligned Sb_2Te_3 (seed) layer, the primary SL growth was attempted according to the optimized process schedule shown in Figure 2-11 (d), determined by several attempts with different process schedules.

The well-alignment of the Sb_2Te_3 single film over the 3D hole structure could be found in Figures 2-12. The preferred crystal orientation of the ALD Sb_2Te_3 film with NH_3 co-injection was maintained on a three-dimensional trench structure, as shown in the cross-sectional TEM images. Trench patterns of 1.0 μm-wide, 0.4 μm-deep were fabricated in CVD SiO_2 film, and the Sb_2Te_3 film was deposited according to the NH_3 co-injected ALD sequence. Interestingly, the ALD Sb_2Te_3 films were grown with their c-axis alignment along the local surface-normal-directions not only on the top and bottom
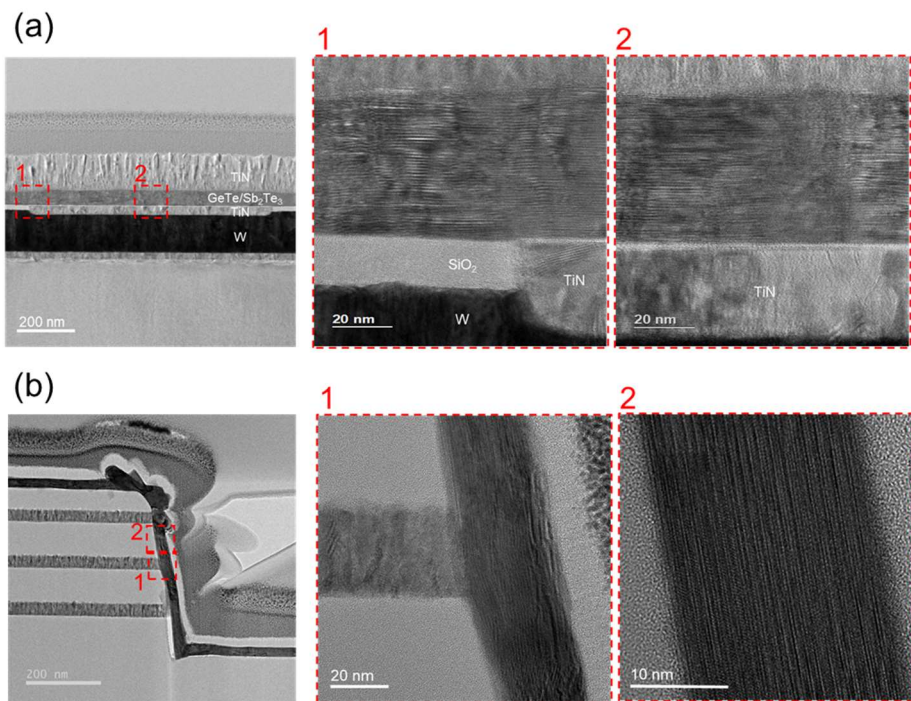
Figure 2-13. Structural characteristics of the planar and vertical devices with the aligned GeTe/Sb$_2$Te$_3$ superlattice. Cross-sectional TEM images of the ALD GeTe/Sb$_2$Te$_3$ superlattice film on an (a) planar and (b) vertical device. The figures with a red border on the right are higher-magnified images of the local phases indicated by the red box and numbers on the left figure.

portion of the substrate but also on the sidewall portions of the trench with conformal film thickness. Unlike physical vapor deposition methods such as sputter and evaporator, ALD technology deposits thin films with the isotropic flow of precursors. It exhibits a unique saturation reaction after the chemical reactions at all sites.[25] This advantage of the ALD technology allows the Sb_2Te_3 film to align even on such sidewall areas, which is critical for fabricating V-PCM devices utilizing the $GeTe/Sb_2Te_3$ SL.

Figure 2-13 shows the cross-sectional TEM images of a planar-/vertical-type device fabricated for electrical measurements utilizing the $GeTe/Sb_2Te_3$ SL deposition and their alignment technique. Figure 2-13 (a) shows the $GeTe/Sb_2Te_3$ SL grown on a planar TiN-plug wafer. The large square TiN plug (800 nm edge length) connected to the bottom W interconnect wire was selected (the actual electrical measurements were carried out on devices with an edge length of 80 nm) to facilitate the TEM. The right two portions show the enlarged images of the SL at the boundary between the SiO_2 and TiN and on the TiN portion, respectively. The homogeneous and continuous SL can be observed irrespective of the types of underlayers. The same conclusion could be achieved from the etched sidewall areas of the vertically integrated test PCM cell in Figure 2-13 (b). The stack structure comprises three 30 nm thick sputtered TiN layers among the 90 nm thick SiO_2 insulating layers. The right portion TEM images confirm that the structure's sidewall areas are coated with the uniform SL layer. As an unavoidable consequence of the *in-situ* crystallized SL growth

mechanism, the upper corner portion contained irregularly shaped film. This part could be removed by appropriate etching or polishing during the integration process.

2. 3. 3. Electrical Performance and Switching Mechanism

The electrical performance was measured for a planar- (mushroom-) and vertical-type PCM cell, where the contact area was 80 x 80 (6400) nm^2 and 500 x 40 (20000) nm^2, respectively. In Figures 2-14 (a) and (b), black square symbol data correspond to the GST225 alloy, which generally shows a gradual increase in resistance with the increasing RESET current. The GST225 alloy was also deposited with ALD by intentionally mixing the Ge, Sb, and Te atoms with repeated short cycles.[15,16] Due to the gradual change of the resistance, defining the I_{RESET} was tricky, but the current value at which the 90% of saturated resistance was taken as the I_{RESET}. For a more quantitative comparison, the I_{RESET} was converted to the RESET current density, J_{RESET}, by dividing the value by the contact area. The J_{RESET} of the ALD GST225 alloy was ~20 MA/cm^2 for both planar- and vertical-type devices, comparable to previous works where similar GST225 films with mushroom-type PCM configuration were tested. Notably, the SL with the planar-type device (red circle data in Figure 14 (a)) showed a J_{RESET} as small as ~ 3 MA/cm^2, only ~1/7 of the GST225 alloy case. The J_{RESET} of this work is considerably lower compared to other reported GSTs, as in Figure 2-14 (c).[26–32] It also shows a much abrupt RESET transition at the critical I_{RESET}. The vertical-type device also significantly decreased the J_{RESET} (5 – 10 MA/cm^2) with an abrupt transition, but the data scattered more severely. This is due to the low quality of the vertical-type device fabrication performed by the university-scale pieces of equipment, whereas the mushroom cell was
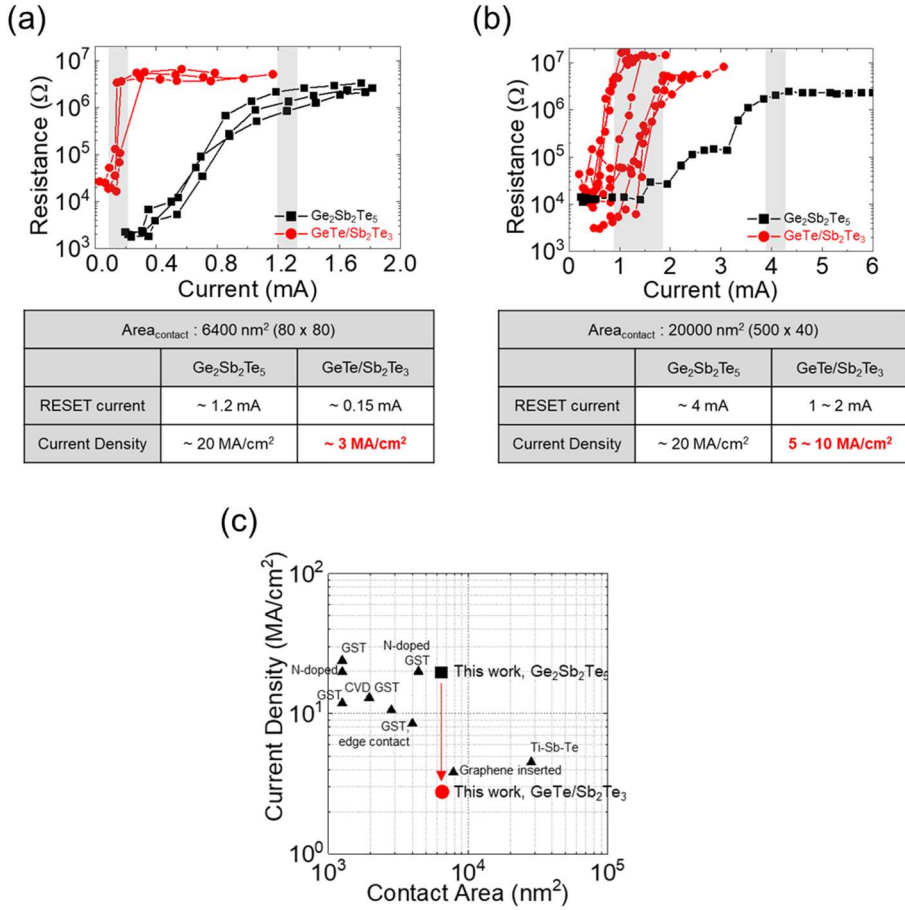
Figure 2-14. (a), (b) Resistance versus current of the planar and vertical device, respectively. Note that the operating area is 80 x 80 and 500 x 40 nm^2. (c) Reset current density versus contact area for various PCMs. The result of GeTe/Sb$_2$Te$_3$ SL from this work is shown in a red circle.

fabricated in mass production lines. Nonetheless, the significantly improved I_{RESET} performance of the SL over the alloy layer PCM was evident.

However, the physical origin of such improved switching performance of the GeTe/Sb$_2$Te$_3$ SL is still under controversy. Understanding the switching mechanism is crucial for further developments based on SLs. The most straightforward method to identify the switching mechanism is to observe the crystal structure of the active region in the operating state. Figures 2-15 and 2-16 show the cross-sectional TEM and FFT images of a mushroom cell with the SL film after the RESET and SET operations, respectively. The device was finalized with the RESET or SET process after repeating the RESET/SET operations by 5×10^3 cycles to ensure statistical accuracy. In the RESET state in Figure 2-15, the SL involved an amorphous region with clear amorphous halo patterns on top of the TiN bottom contact electrode, as shown in the FFT images. The dome-shaped amorphous region is marked with a red dashed line in Figure 2-15 (a), which indicates the active region of the cell. This demonstrates that the resistance switching of the SL from low- to high-resistance state operates through the conventional crystalline–amorphous transition, in contrast to the commonly stated crystalline–crystalline transition in IPCM.[1] Interestingly, there are additional crystal regions with FCC GST structure between the amorphous dome and the SL structure far away from the dome region. The 111-planes (originally 001-planes in hexagonal SL, but intermixed and formed FCC 111-planes) of the FCC GST are aligned parallel to the substrate. This FCC
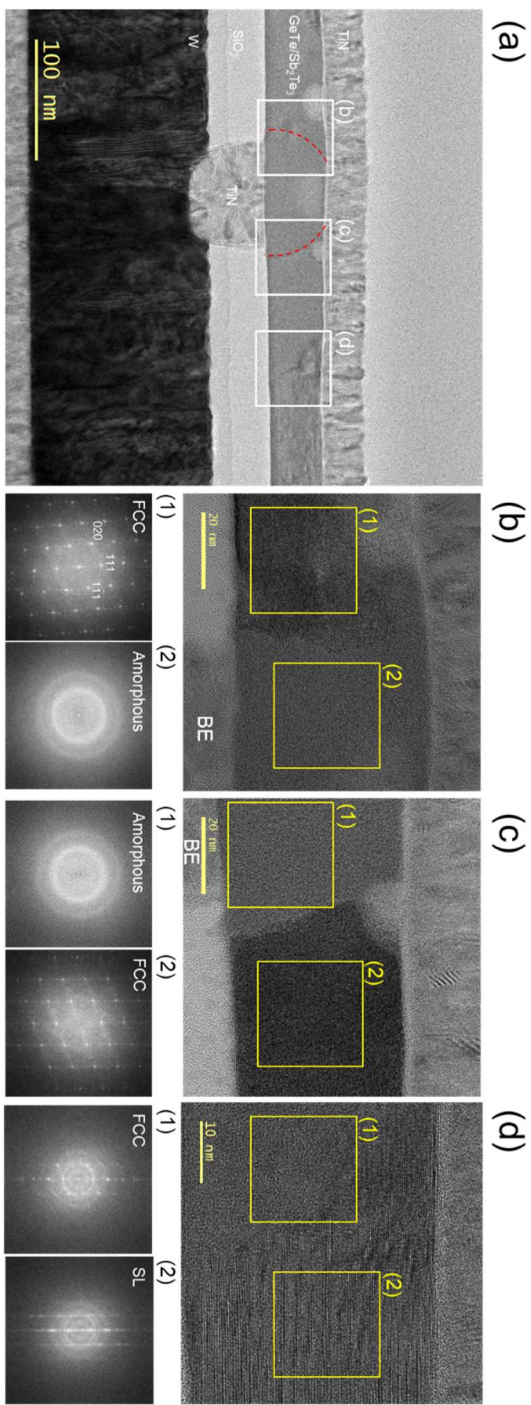
Figure 2-15. (a) Cross-sectional TEM images of the GeTe/Sb$_2$Te$_3$ SL structure in the RESET state after 5x10^3 cycles. (b)-(d) are high-magnified TEM and FFT images of the local phases indicated by the white box on figure (a).
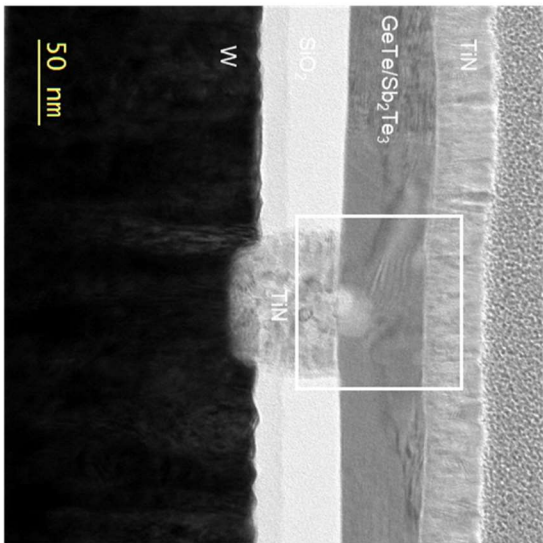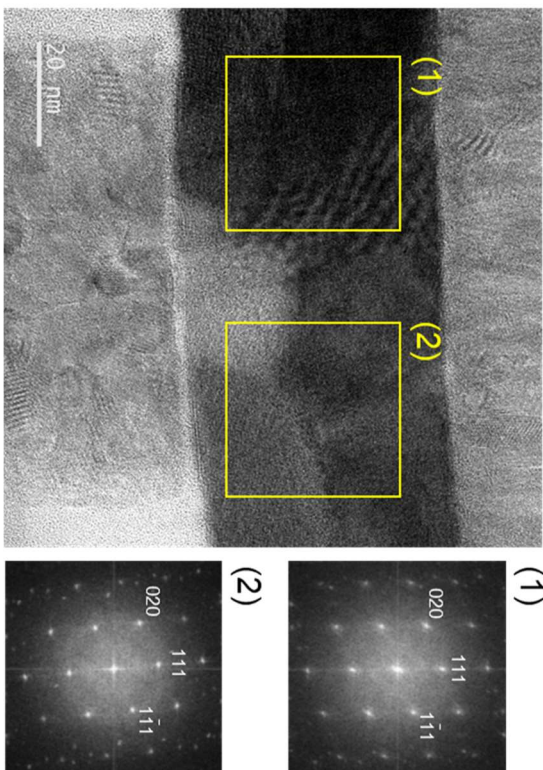
Figure 2-16. (a) Cross-sectional TEM images of the $GeTe/Sb_2Te_3$ SL structure in the SET state after 5×10^3 cycles. (b) is a high-magnified TEM and FFT image of the local phase indicated by the white box on figure (a).
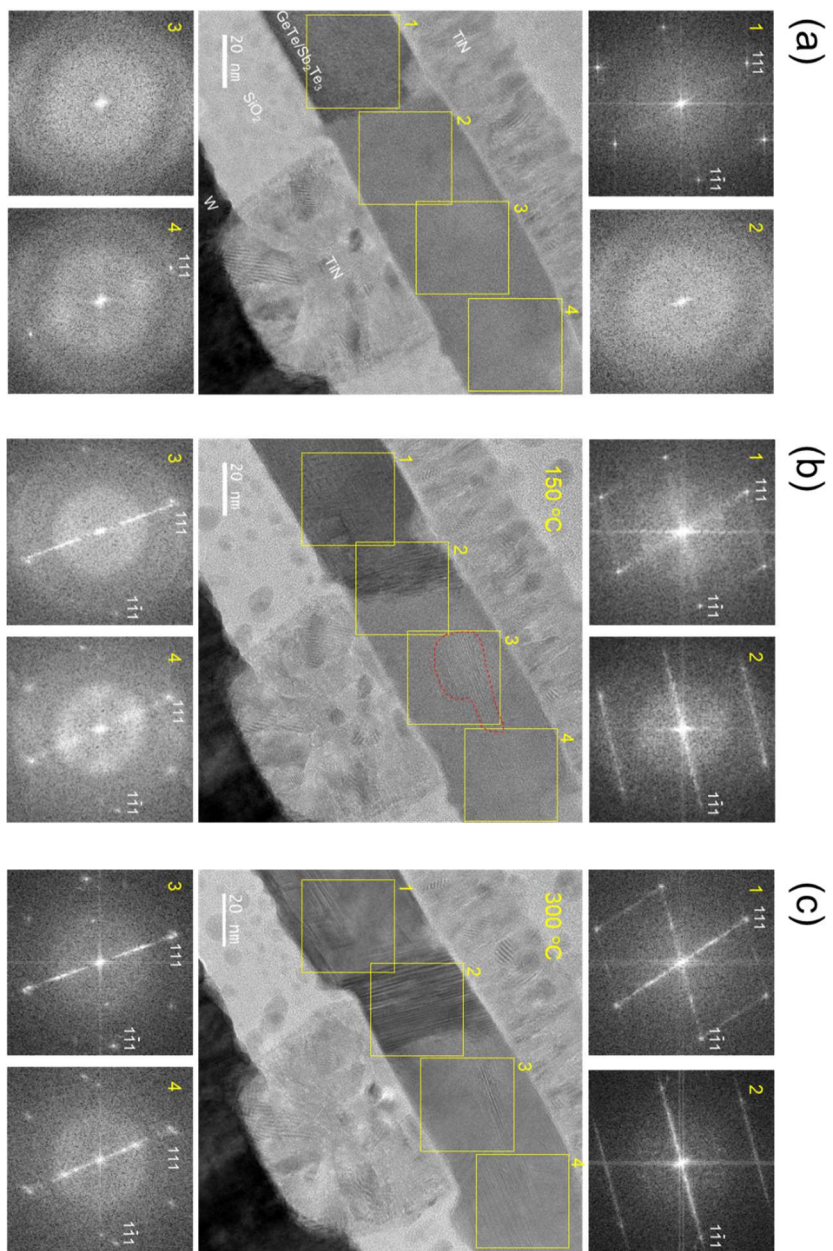
Figure 2-17. Cross-sectional TEM and FFT images during *in-situ* heating using the RESET state sample (same sample used in Figure 2-15). (a) Before heating, (b) 150 $^\circ$C, (c) 300 $^\circ$C heated.

46

structures are formed by the intermixing of the SL structures, possibly by electrical stress. This is because the thermal stress by annealing the SL forms a hexagonal $Ge_2Sb_2Te_5$ alloy, not FCC (confirmed by XRD). Interestingly, these aligned FCC GSTs appear in the recrystallized active region after the SET process, as shown in the TEM images in Figure 2-16. As seen in the high-magnified TEM and FFT images of the local phases in Figure 2-16 (b), the diffraction pattern of the recrystallized active region corresponds to the 111-planes parallel to the substrate. Considering that the crystallinity after the SET process appears randomly in conventional PCM devices, the 111-plane orientation stored after the SET process with 5×10^3 cycles of switching is an exceptional case. This indicates that the amorphous phase in the RESET state stores certain ordered clusters, as only the relatively ordered amorphous structures can crystallize back to the same orientation.

Similar results indicated that the amorphous phase stores certain ordered clusters in *in-situ* heating TEM, as shown in Figures 2-17. The $GeTe/Sb_2Te_3$ SL crystal structure was analyzed by heating *in-situ* inside the TEM chamber using the same RESET state sample used in Figure 2-15. The amorphous phase started to crystallize at a temperature of 150 °C (Figure 2-17 (b)) and was fully crystallized at a sufficiently high temperature of 300 °C (Figure 2-17 (c)). It should be noted that the growth-dominant grains from the already crystallized phases and also the newly nucleated grains inside the amorphous phase (indicated by the red line in Figure 2-17 (b)) are aligned in a specific orientation

47
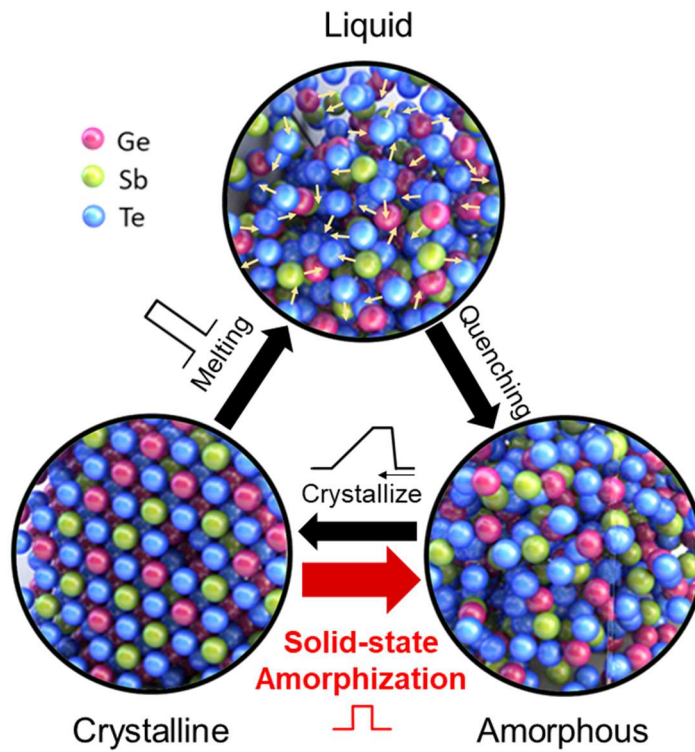
Figure 2-18. Schematic diagram of the phase transition pathway of phase change materials. The direct solid-state amorphization without 'melting' and 'quenching' can be achieved.

of 111-plane alignment, parallel to the substrate. This could further support that the amorphous phase in the RESET state certainly has an ordered structure. The fact that the amorphous state 'stores' the atomic arrangement information of the crystalline state indicates that the atomic displacement during amorphization is relatively low.

Figure 2-18 shows a schematic diagram of the phase transition pathway of a phase-change material. Conventional amorphization is made by applying a large electrical pulse for a short time, allowing amorphization *via* melting and subsequent quenching. Although short-lived, this process involves a liquid phase and therefore cannot 'store' the atomic arrangement information by the active mixing of the atoms. Meanwhile, several studies have shown that solid-state amorphization (SSA), which does not involve a liquid phase, can occur by various methods such as pressure,[33-36] magnetic field,[37] e-beam irradiation,[38] and photoexcitation.[39] The amorphous structure by the SSA is known to contain more information about the crystalline state due to the absence of the melting process. In particular, the characteristic nature of FCC GST225 may lead to pressure-induced amorphization, mainly due to the large number of 20 % vacancies in the Ge/Sb-sites. Here, we propose an SSA process for low-current amorphization of the SL film based on the fact that the SL stores an ordered crystal motif at the RESET state.
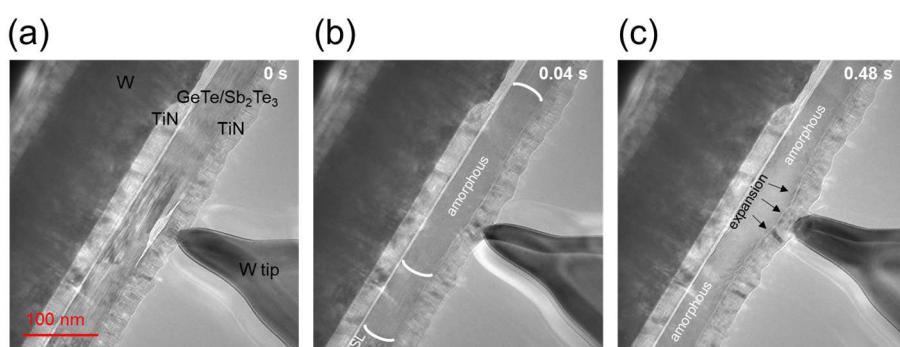
Figure 2-19. Cross-sectional TEM images of *in-situ* biasing. (a) Before, (b) 0.04 s, (c) 0.48 s.

The *in-situ* biasing TEM can observe the SSA process as in Figure 2-19. The sample was set with a W tip on the top and bottom electrode in the TEM chamber. Change in the GeTe/Sb$_2$Te$_3$ SL structure with time was observed while applying the electrical field. At 0.04 s (Figure 2-19 (b)), an amorphous structure was formed without any volume change. By applying more electrical fields, at 0.48 s, the film expands (Figure 2-19 (c)). The conventional melt-quenching process accompanies a volume expansion due to the formation of a liquid phase, meaning that the amorphization at 0.04 s can be estimated as an SSA process. At 0.48 s, a sufficient electrical field to melt the film was applied, and the film volume expanded. The appearance of the SSA process in GeTe/Sb$_2$Te$_3$ SL devices seems quite apparent.

Then, it is necessary to understand why the SSA occurs only in the GeTe/Sb$_2$Te$_3$ SL, which wasn't the case in the conventional GST alloys. It seems that a significant amount of compression stress is generated in the FCC GST 111 aligned structure, which appeared around the active region in the SET and RESET state (Figures 2-15 and 2-16). The conversion from GeTe/Sb$_2$Te$_3$ SL to FCC GST by electrical stress forms random voids, and the bulk density is lowered.[40] The volume will expand, thus creates compression stress around it. Careful estimation of the *d*-spacing from the FFT images showed a compressive strain in the direction of the 111-plane. It was confirmed by the different *d*-spacing of the 111 and $1\bar{1}1$-planes. Although the compressive strain measurement using the *d*-spacing by TEM is inaccurate due to the small

Bragg angle in TEM, the compression stress was estimated to be about 600 MPa. The following (1)–(4) equations of Mohr's circle, Young's modulus of 40 GPa, and Poisson's ratio of 0.3 are used.

$$\sigma_x = 0, \ \sigma_y = \sigma_z = -\sigma \tag{1}$$

$$\varepsilon_x = \frac{1}{Y}\{\sigma_x - \nu(\sigma_y + \sigma_z)\} = \frac{2\nu}{Y}\sigma, \qquad \varepsilon_y = \frac{1}{Y}\{\sigma_y - \nu(\sigma_z + \sigma_x)\} = -\frac{\sigma}{Y}(1 - \nu) \tag{2}$$

$$R = \frac{\sigma}{2Y}(1 + \nu), \ center: (\frac{3\nu - 1}{2Y}\sigma, 0) \tag{3}$$

$$\varepsilon_{111} = \frac{2\nu}{Y}\sigma, \qquad \varepsilon_{1\bar{1}1} = \frac{1}{2Y}\sigma\{(3 + \cos 2\theta)\nu - (1 - \cos 2\theta)\} \tag{4}$$

The significant amount of compression stress being applied in the active region is also shown in Figure 2-17. By the elevated temperature of 150 and 300 °C, the atoms migrated from the amorphous region to the adjacent part, and the thickness of the film around the bottom electrode became thicker. The significant migration of the film indicates that a considerable amount of compression stress is being applied to the active region.

Meanwhile, the commonly stated umbrella-flip switching mechanism in phase-change material was first proposed by Kolobov et al.[41] The order-disorder transition is formed by an umbrella flipping of Ge atoms from an octahedral position into a tetrahedral position without rupture of strong covalent bonds. Considering this, the Ge flipping model can explain the pressure-induced SSA of the GeTe/Sb$_2$Te$_3$ SL device, which can be referred to as an
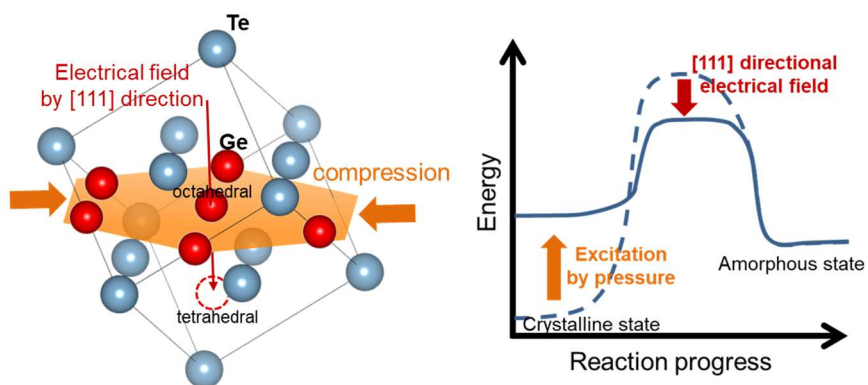
Figure 2-20. Schematic summary of the pressure-induced solid-state amorphization process.

enhanced flipping model. The presence of significant compression stress in the 111-plane, which is a closed-packed plane, can enhance the migration of the Ge atoms. With the excited energy by the compression stress, the electrical field (RESET pulse) triggers the migration of the Ge atoms from an octahedral to a tetrahedral site. The electrical field is oriented in the 111-direction, in which the Ge atom should migrate so that the electrical field can trigger the Ge movement more efficiently. This pressure-induced SSA process is summarized in Figures 2-20. First, the FCC GST structure is aligned along the 111-direction. The energy of the crystalline state is excited by the compression stress in the 111-plane, and the efficient 111-directional electrical field triggers the Ge to umbrella-flip from the octahedral to the tetrahedral site. This could certainly lower the current to induce amorphization. The pressure-induced solid-state amorphization is not yet clear; however, it can help understand the nature of the resistive switching mechanism in low-current operating $GeTe/Sb_2Te_3$ SL.

2.4. Conclusion

In conclusion, well-aligned and crystallized GeTe/Sb$_2$Te$_3$ SL films were grown on horizontal and vertical surfaces by the atomic layer deposition. The solid chemical affinity of Sb atoms toward the SiO$_2$ and TiN surfaces allowed the formation of the first Sb-monolayers on both materials. The subsequent chemical adsorption of Te-precursor molecules *via* the ALD-specific ligand exchange reaction naturally resulted in the entirely c-axis-aligned Sb$_2$Te$_3$ layers. Such a c-axis-aligned Sb$_2$Te$_3$ could serve as the seed for the *in-situ* crystallized 111-direction aligned GeTe layer, which would have been either amorphous or randomly oriented polycrystalline layer if it was directly grown on the SiO$_2$ and TiN surfaces. The RESET current of the superlattice film decreased to ~ 1/7 of Ge$_2$Sb$_2$Te$_5$ randomly-oriented alloy films in the conventional mushroom-type and the sidewall-type vertical PCM cell. The fluent improvement in the resistance switching performance from this GeTe/Sb$_2$Te$_3$ SL originates from the pressure-induced solid-state amorphization, not from the crystalline–crystalline transition of the IPCM. This could be a step forward improvement for fabricating the futuristic vertical-type PCM with low operating power, which may succeed in the current vertical-NAND flash memory and SCM.

2.5. References

(1)   Simpson, R. E.; Fons, P.; Kolobov, A. V.; Fukaya, T.; Krbal, M.; Yagi, T.; Tominaga, J. Interfacial Phase-Change Memory. *Nat. Nanotechnol.* **2011**, *6* (8), 501–505.

(2)   Tominaga, J. The Design and Application on Interfacial Phase-Change Memory. *Phys. Status Solidi - Rapid Res. Lett.* **2019**, *13* (4), 1–11.

(3)   Boniardi, M.; Boschker, J. E.; Momand, J.; Kooi, B. J.; Redaelli, A.; Calarco, R. Evidence for Thermal-Based Transition in Super-Lattice Phase Change Memory. *Phys. Status Solidi - Rapid Res. Lett.* **2019**, *13* (4), 1–6.

(4)   Térébénec, D.; Castellani, N.; Bernier, N.; Sever, V.; Kowalczyk, P.; Bernard, M.; Cyrille, M. C.; Tran, N. P.; Hippert, F.; Noé, P. Improvement of Phase-Change Memory Performance by Means of GeTe/Sb$_2$Te$_3$ Superlattices. *Phys. Status Solidi - Rapid Res. Lett.* **2021**, *15* (3), 1–9.

(5)   Li, X. Bin; Chen, N. K.; Wang, X. P.; Sun, H. B. Phase-Change Superlattice Materials toward Low Power Consumption and High Density Data Storage: Microscopic Picture, Working Principles, and Optimization. *Adv. Funct. Mater.* **2018**, *28* (44), 1–21.

(6)   Zhang, W.; Mazzarello, R.; Wuttig, M.; Ma, E. Designing Crystallization in Phase-Change Materials for Universal Memory and Neuro-Inspired Computing. *Nat. Rev. Mater.* **2019**, *4* (3), 150–168.

(7)   Wuttig, M.; Yamada, N. Phase Change Materials for Rewriteable Data Storage. *Nat. Mater.* **2007**, *6*, 824–832.

(8)   Wong, H.-S. P.; Raoux, S.; Kim, S.; Liang, J.; Reifenberg, J. P.; Rajendran, B.; Asheghi, M.; Goodson, K. E. Phase Change Memory. *Proc. IEEE* **2010**, *98* (12),

2201–2227.

(9)   Burr, G. W.; BrightSky, M. J.; Sebastian, A.; Cheng, H.-Y.; Wu, J.-Y.; Kim, S.;
        Sosa, N. E.; Papandreou, N.; Lung, H.-L.; Pozidis, H.; Eleftheriou, E.; Lam, C.
        H. Recent Progress in Phase-Change Memory Technology. *IEEE J. Emerg. Sel.*
        Top. Circuits Syst. **2016**, *6* (2), 1–17.

(10)   Boschker, J. E.; Lü, X.; Bragaglia, V.; Wang, R.; Grahn, H. T.; Calarco, R.
        Electrical and Optical Properties of Epitaxial Binary and Ternary GeTe-Sb$_2$Te$_3$
        Alloys. *Sci. Rep.* **2018**, *8* (1), 1–8.

(11)   Momand, J.; Lange, F. R. L.; Wang, R.; Boschker, J. E.; Verheijen, M. A.;
        Calarco, R.; Wuttig, M.; Kooi, B. J. Atomic Stacking and Van-Der-Waals
        Bonding in GeTe-Sb$_2$Te$_3$ Superlattices. *J. Mater. Res.* **2016**, *31* (20), 3115–3124.

(12)   Wang, R.; Bragaglia, V.; Boschker, J. E.; Calarco, R. Intermixing during
        Epitaxial Growth of van Der Waals Bonded Nominal GeTe/ Sb$_2$Te$_3$
        Superlattices. *Cryst. Growth Des.* **2016**, *16* (7), 3596–3601.

(13)   Jiang, Z.; Qin, S.; Li, H.; Fujii, S.; Lee, D.; Wong, S.; Philip Wong, H. S. P.
        Next-Generation Ultrahigh-Density 3-D Vertical Resistive Switching Memory
        (VRSM)-Part II: Design Guidelines for Device, Array, and Architecture. *IEEE*
        Trans. Electron Devices **2019**, *66* (12), 5147–5154.

(14)   Qin, S.; Jiang, Z.; Li, H.; Fujii, S.; Lee, D.; Simon Wong, S.; Wong, H. S. P.
        Next-Generation Ultrahigh-Density 3-D Vertical Resistive Switching Memory
        (VRSM)-Part I: Accurate and Computationally Efficient Modeling. *IEEE Trans.*
        Electron Devices **2019**, *66* (12), 5139–5146.

(15)   Park, E. S.; Yoo, C.; Kim, W.; Ha, M.; Jeon, J. W.; Lee, Y. K.; Hwang, C. S.
        Developing Precursor Chemistry for Atomic Layer Deposition of High-Density,
        Conformal GeTe Films for Phase-Change Memory. *Chem. Mater.* **2019**, 31 (21),

8663-8672.

(16)   Park, E.-S.; Yoo, C.; Kim, W.; Ha, M.; Jeon, J. W.; Eom, T.; Lee, Y. K.; Hwang, C. S. Atomic Layer Deposition of Nanocrystalline-As-Deposited $(GeTe)_x(Sb_2Te_3)_{1-x}$ Films for Endurable Phase Change Memory. *Chem. Mater.* **2019**, *31* (21), 8752–8763.

(17)   Lee, Y. K.; Yoo, C.; Kim, W.; Jeon, J. W.; Hwang, C. S. Atomic Layer Deposition of Chalcogenides for Next-Generation Phase Change Memory. *J. Mater. Chem. C* **2021**, *9* (11), 3708–3725.

(18)   Boschker, J. E.; Tisbi, E.; Placidi, E.; Momand, J.; Redaelli, A.; Kooi, B. J.; Arciprete, F.; Calarco, R. Textured Sb_2Te_3 Films and GeTe/ Sb_2Te_3 Superlattices Grown on Amorphous Substrates by Molecular Beam Epitaxy. *AIP Adv.* **2017**, *7* (1), 015106.

(19)   Saito, Y.; Fons, P.; Bolotov, L.; Miyata, N.; Kolobov, A. V.; Tominaga, J. A Two-Step Process for Growth of Highly Oriented Sb_2Te_3 Using Sputtering. *AIP Adv.* **2016**, *6* (4), 2–7.

(20)   Saito, Y.; Fons, P.; Kolobov, A. V.; Tominaga, J. Self-Organized van Der Waals Epitaxy of Layered Chalcogenide Structures. *Phys. Status Solidi Basic Res.* **2015**, *252* (10), 2151–2158.

(21)   Simpson, R. E.; Fons, P.; Kolobov, A. V.; Krbal, M.; Tominaga, J. Enhanced Crystallization of GeTe from an Sb_2Te_3 Template. *Appl. Phys. Lett.* **2012**, *100* (2), 3–7.

(22)   Cecchi, S.; Zallo, E.; Momand, J.; Wang, R.; Kooi, B. J.; Verheijen, M. A.; Calarco, R. Improved Structural and Electrical Properties in Native $Sb_2Te_3/Ge_xSb_2Te_{3+x}$ van Der Waals Superlattices Due to Intermixing Mitigation. *APL Mater.* **2017**, *5* (2), 1–7.

(23)   Chen, N.; Li, X.; Wang, X.; Xie, S.; Tian, W. Q. Metal–Insulator Transition of Ge–Sb–Te Superlattice : An Electron Counting Model Study. **2018**, *17* (1), 140–146.

(24)   Kooi, B. J.; Momand, J. High Resolution Imaging of Chalcogenide Superlattices for Data Storage Applications: Progress and Prospects. *Phys. Status Solidi - Rapid Res. Lett.* **2019**, *13* (4), 1–13.

(25)   George, S. M. Atomic Layer Deposition: An Overview. *Chem. Rev.* **2010**, *110* (1), 111-131.

(26)   Neumann, C. M.; Okabe, K. L.; Yalon, E.; Grady, R. W.; Wong, H. S. P.; Pop, E. Engineering Thermal and Electrical Interface Properties of Phase Change Memory with Monolayer MoS_2. *Appl. Phys. Lett.* **2019**, *114* (8).

(27)   Wu, J. Y.; Chen, Y. S.; Khwa, W. S.; Yu, S. M.; Wang, T. Y.; Tseng, J. C.; Chih, Y. D.; Diaz, C. H. A 40 nm Low-Power Logic Compatible Phase Change Memory Technology. *Tech. Dig. - Int. Electron Devices Meet. IEDM* **2019**, *2018-Decem*, 27.6.1-27.6.4.

(28)   Cheng, H. Y.; Wu, J. Y.; Cheek, R.; Raoux, S.; Brightsky, M.; Garbin, D.; Kim, S.; Hsu, T. H.; Zhu, Y.; Lai, E. K.; Joseph, E.; Schrott, A.; Lai, S. C.; Ray, A.; Lung, H. L.; Lam, C. A Thermally Robust Phase Change Memory by Engineering the Ge/N Concentration in $(Ge, N)_x Sb_y Te_z$ Phase Change Material. *Tech. Dig. - Int. Electron Devices Meet. IEDM* **2012**, 725–728.

(29)   Chao, D. S.; Hsu, H. H.; Chen, M. J.; Chen, Y. C.; Chen, F.; Lee, C. M.; Yen, P. H.; Chen, C. W.; Wang, W. H.; Chen, W. S.; Lien, C.; Kao, M. J.; Tsai, M. J. Low Programming Current Phase Change Memory Cell with Double GST Thermally Confined Structure. *Int. Symp. VLSI Technol. Syst. Appl. Proc.* **2007**, 7–8.

(30)   Lee, J. I.; Park, H.; Cho, S. L.; Park, Y. L.; Bae, B. J.; Park, J. H.; Park, J. S.;
         An, H. G.; Bae, J. S.; Ahn, D. H.; *et al.* Highly Scalable Phase Change Memory
         with CVD GeSbTe for Sub 50 nm Generation. *Dig. Tech. Pap. - Symp. VLSI
         Technol.* **2007**, 102–103.

(31)   Ding, K.; Rao, F.; Lv, S.; Cheng, Y.; Wu, L.; Song, Z. Low-Energy
         Amorphization of $Ti_1Sb_2Te_5$ Phase Change Alloy Induced by $TiTe_2$ Nano-
         Lamellae. *Sci. Rep.* **2016**, 6, 30645.

(32)   Zhu, M.; Xia, M.; Rao, F.; Li, X.; Wu, L.; Ji, X.; Lv, S.; Song, Z.; Feng, S.; Sun,
         H.; Zhang, S. One Order of Magnitude Faster Phase Change at Reduced Power
         in Ti-Sb-Te. *Nat. Commun* **2014**, *5*, 4086.

(33)   Kolobov, A. V.; Haines, J.; Pradel, A.; Ribes, M.; Fons, P.; Tominaga, J.;
         Katayama, Y.; Hammouda, T.; Uruga, T. Pressure-Induced Site-Selective
         Disordering of $Ge_2Sb_2Te_5$: A New Insight into Phase-Change Optical
         Recording. *Phys. Rev. Lett.* **2006**, *97* (3), 2–5.

(34)   Kolobov, A. V.; Haines, J.; Pradel, A.; Ribes, M.; Fons, P.; Tominaga, J.;
         Steimer, C.; Aquilanti, G.; Pascarelli, S. Pressure-Induced Amorphization of
         Quasibinary $GeTe-Sb_2Te_3$: The Role of Vacancies. *Appl. Phys. Lett.* **2007**, *91*
         (2), 10–13.

(35)   Krbal, M.; Kolobov, A. V.; Hanfland, M.; Fons, P. Crystallization of $Ge_2Sb_2Te_5$
         under High Hydrostatic Pressures: Differences in Nanoscale Atomic Ordering
         in as-Deposited and Pressure-Induced Amorphous Phases. *J. Alloys Compd.*
         2021, *874*, 159980.

(36)   Xu, K.; Miao, X.; Xu, M. The Structure of Phase-Change Chalcogenides and
         Their High-Pressure Behavior. *Phys. Status Solidi - Rapid Res. Lett.* **2019**, *13*
         (4), 1–14.

(37) Tominaga, J.; Bolotov, L. Re-Amorphization of GeSbTe Alloys Not through a Melt-Quenching Process. *Appl. Phys. Express* **2019**, *12* (1).

(38) Jiang, T. T.; Wang, J. J.; Lu, L.; Ma, C. S.; Zhang, D. L.; Rao, F.; Jia, C. L.; Zhang, W. Progressive Amorphization of GeSbTe Phase-Change Material under Electron Beam Irradiation. *APL Mater.* **2019**, *7* (8).

(39) Fons, P.; Osawa, H.; Kolobov, A. V.; Fukaya, T.; Suzuki, M.; Uruga, T.; Kawamura, N.; Tanida, H.; Tominaga, J. Photoassisted Amorphization of the Phase-Change Memory Alloy $Ge_2Sb_2Te_5$. *Phys. Rev. B - Condens. Matter Mater. Phys.* **2010**, *82* (4), 1–4.

(40) Njoroge, W. K.; Wöltgens, H.-W.; Wuttig, M. Density Changes upon Crystallization of $Ge_2Sb_{2.04}Te_{4.74}$ Films. *J. Vac. Sci. Technol. A Vacuum, Surfaces, Film.* **2002**, *20* (1), 230–233.

(41) Kolobov, A. V.; Fons, P.; Frenkel, A. I.; Ankudinov, A. L.; Tominaga, J.; Uruga, T. Understanding the Phase-Change Mechanism of Rewritable Optical Media. *Nat. Mater.* **2004**, *3*, 703–708.

3. Atomic Layer Deposition of Ge$_x$Se$_{1-x}$ Thin Films for Endurable Ovonic Threshold Selectors with a Low Threshold Voltage

3.1. Introduction

Emerging non-volatile memories (NVMs), including phase-change memory (PCM), resistive random access memory (RRAM), and magnetic random access memory (MRAM), store information using distinctive resistance states that are dependent on the physicochemical state of the cell.[1–3] A crossbar array (CBA) architecture with these memories allows for low-cost, CMOS-compatible fabrication of high-density, high-performance memories. In particular, the passive matrix structure of the CBAs requires only an effective footprint of 4F^2 per cell, where F means the minimum feature size.[4] Selector devices are an essential element in such CBA structure to access a certain memory cell without misleading sneak currents.[5] Among several options for a selector, the ovonic threshold switch (OTS) based on amorphous chalcogenide materials is a promising candidate for their capabilities of a high ON current and fast switching speed. OTS is a bidirectional switch device that undergoes a sudden volatile transition to a low resistance state above a certain critical bias.[6,7] Among several options for chalcogenide-based OTS, GeSe is attractive due to its environment-friendly and simple binary composition with high thermal

stability with a crystalline temperature of ~380 °C.[8–13] Previous studies successfully demonstrated the use of a 1S-1R structure, which consists of stacked layers of GeSe as the selector and PCM, RRAM, and MRAM as the resistive memory layer.[14–17]

However, previous studies on GeSe OTS have mostly adopted physical vapor deposition methods that have limitations in constructing high-aspect-ratio architectures due to their poor step coverage. Although the current realization of high-density CBA including 3D X-point[18] produced by Intel, relies on stacking the planar layers of the selector and resistor elements, the fabrication of such structure prevents a further increase in memory capacity due to linearly increasing processing steps and areas for periphery interconnecting wires with the number of stacking layers. A vertical NAND (V-NAND) flash type architecture can be an alternative to achieve an efficient increase in the integration density of the CBAs without causing such fabrication and design problems.[19,20] The V-NAND architecture uses far fewer lithography steps during the fabrication of high-density memory, but conformal deposition of thin-film materials on vertical sidewalls must be achieved for its construction.

Atomic layer deposition (ALD) offers conformality and atomic-level accuracy due to its unique self-limiting growth.[21–23] In general, ALD deposits oxide materials such as Al_2O_3 and TiO_2 by injecting and purging a specific precursor with a reactant gas such as H_2O or O_3. Meanwhile, chalcogenide-

based OTS must be deposited through a ligand exchange reaction between different precursors. The recent development of precursor design and synthesis enabled the ALD of various chalcogenide materials for PCM and OTS.[24–30] The authors' group reported the ALD process of GeSe[31] or Ge-Sb-Se-Te[32] films for the OTS device using precursors including $HGeCl_3$, $Sb(OC_2H_5)_3$, and $((CH_3)_3Si)_2Se$. The simple binary composition of GeSe is attractive, but their cycle endurance was limited to being below 10^3 cycles due to their high impurity and surface oxidation issues. Further issues resulting from the chloride-based chemistry of the Ge precursor, including the long-term stability, contamination, and Cl-induced etch problems, were potential limitations to the mass production of these films.

This paper reports on the thermal ALD behavior of a GeSe binary compound adopting $Ge(N(Si(CH_3)_3)_2)_2$ and $((CH_3)_3Si)_2Se$ precursors with methanol co-injection. The $Ge(N(Si(CH_3)_3)_2)_2$ precursor was previously utilized to deposit Ge-Te thin films through a combination with $((CH_3)_3Si)_2Te$ as the Te source by the authors' research group.[33] Motivated by the interesting chemistries and excellent physical/chemical qualities of the film, the present study replaced the Te precursor with $((CH_3)_3Si)_2Se$ to obtain Ge-Se films for OTS applications with advanced electrical characteristics compared to that of previous GeSe films formed by ALD using $HGeCl_3$ as a Ge source.[31] The Ge-Se film was feasibly deposited with ALD saturation behavior, and the Ge

contents were varied by varying the growth temperature and the Ge precursor injection time.

The OTS performance was tested by fabricating a mushroom-type device. A low threshold voltage of 1.2 V was achieved, which could be attributed to the presence of carbon impurities, and a sufficient half-bias nonlinearity of 10^5 and a high cycle endurance of 10^5 were achieved from the 40-nm-thick $Ge_{0.5}Se_{0.5}$ film. The endurance was further improved to 10^6 cycles by changing the composition to $Ge_{0.6}Se_{0.4}$. Considering the availability of ALD of phase change materials, including crystalline-as-deposited $Ge_2Sb_2Te_5$ developed by the authors' research group, the results presented here show the potential usage of ALD to fabricate 3D vertical-type one selector-one resistor (1S-1R) memory for high-density CBAs.[29]

3.2. Experimental

The deposition was performed using a shower-head-type ALD reactor with a 6-inch wafer-scale (CN-1, Atomic-premium). The Ge and Se precursors were $Ge(N(Si(CH_3)_3)_2)_2$ and $((CH_3)_3Si)_2Se$, respectively, as shown in Figure 3-1. Each precursor was contained in a stainless canister at 70 and 30 °C to control the injection rate. The Ge-Se film was deposited with co-injection of methanol gas to form highly reactive intermediates that follow the same mechanism as suggested in the previous report on Ge-Te film deposition.[33] The methanol reacts with Ge- and Se- precursors and forms reactive intermediates, such as $Ge(OCH_3)_2$ and H_2Se. Because of the high vapor pressure of methanol, it was kept at room temperature without heating, and the injection rate was controlled by a metering valve. The Ge- and Se- precursor vapors were carried into the ALD reactor with 100, 50 standard cubic centimeters per minute (sccm) of Ar carrier gas, while methanol was carried with 200 sccm. To purge excess precursors and byproducts, 200 sccm Ar gas was injected right after the precursor injection sequence. 100-nm thick SiO_2/Si and 50nm-thick TiN/SiO_2/Si were used as substrates, where SiO_2 and TiN films were prepared by dry oxidation and sputtering (Applied Materials, Endura 5500), respectively. Every gas flow line was maintained at 100 °C to avoid condensation of the evaporated precursor. The chamber's base and working pressures are 23 mTorr and 2.0-2.5 Torr, respectively.
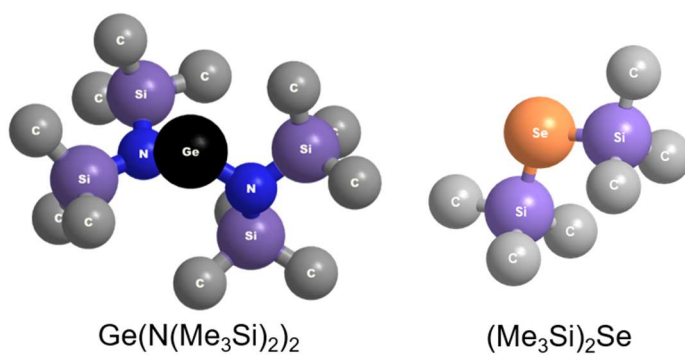
Figure 3-1. Ge(N(Si(CH₃)₃)₂)₂ and ((CH₃)₃Si)₂Se precursor for Ge-Se ALD.

Energy-dispersive X-ray fluorescence (EDXRF, Thermo Scientific, Quant'X) was used to measure the composition and layer density of the deposited films. The crystallinity and the bulk density of the films were measured using X-ray diffraction (XRD) and X-ray reflectivity (XRR) using an X-ray diffractometer (PANalytical, X'Pert PRO MPD). The thickness was confirmed by dividing the layer density by the bulk density and was crosschecked using spectroscopic ellipsometry (SE, J. A. Woolam, ESM-300). Atomic force microscopy (AFM, JEOL, JSPM 5200) was used to inspect the surface morphology of the films. Auger electron spectroscopy (AES, ULVAC-PHI, PHI-700) produced the depth profile of the light element impurity, and X-ray photoelectron spectroscopy (XPS, Kratos, Axis Supra) was performed to confirm the chemical states of the elements in the Ge_xSe_{1-x} film. Cross-sectional transmission electron microscopy (TEM, JEOL, JEM-2100F) using a specimen prepared with a focused ion beam (FEI, Helios 650) and scanning electron microscopy (SEM, Hitachi, S-4800) were used for imaging the Ge_xSe_{1-x} film conformality.

The devices used for electrical characterization were fabricated on a single hole-patterned substrate. The W/Ge-Se/TiN selector device was integrated into a process flow where the W bottom electrode has been patterned as a pillar, with a contact diameter of 135 nm. Ge_xSe_{1-x} films were deposited to a thickness of ~40 nm. A current sourced pulse generator (PG, Agilent, 81110A) was used to apply the electric pulse, and an oscilloscope (OCS, Tektronix, TDS

684C) was used to observe the response of the device. The current-voltage (I-V) characteristics under a DC voltage sweep were measured using a semiconductor parameter analyzer (SPA, Hewlett Packard 4145B).

3.3. Results and Discussions

The chemical structures for $Ge(N((CH_3)_3Si)_2)_2$ and $((CH_3)_3Si)_2Se$ are depicted in Figure 3-1. The typical ALD sequence that alternatively injects the Ge and Se precursors failed to deposit the GeSe films because of the limited reactivity of the precursors towards ligand exchange to form the $((CH_3)_3Si)_2N$-$Si(CH_3)_3$. Figures 3-2 (a) and (b) compare the typical and modified ALD sequences for the Ge-Se deposition, respectively, where the latter sequence involves methanol co-injection with both precursors. The typical ALD sequence consists of 'Ge injection – Ge purge – Se injection – Se purge' whereas the modified sequence injects methanol before, during, and after the precursor injection by using the sequence of 'methanol injection – Ge precursor/methanol co-injection − methanol injection − Ge purge − methanol injection – Se precursor/methanol co-injection – Se purge'. The methanol injection started 3s before the Ge and Se precursor injection and was continuously co-injected with each precursor. The methanol injection was maintained 5s longer after the Ge injections had been stopped. The modified sequence mitigates the passivation effect of the Ge precursor on the substrate and enhances the reactivity of the Ge and Se precursors, as described subsequently. The GeSe film grew only with the modified ALD sequence with methanol co-injection, similar to the previous report of GeTe deposition using the same Ge precursor.[33] Previous reports on GeTe ALD that utilized the same type of Ge precursor suggested that methanol co-injection can prevent strong

70
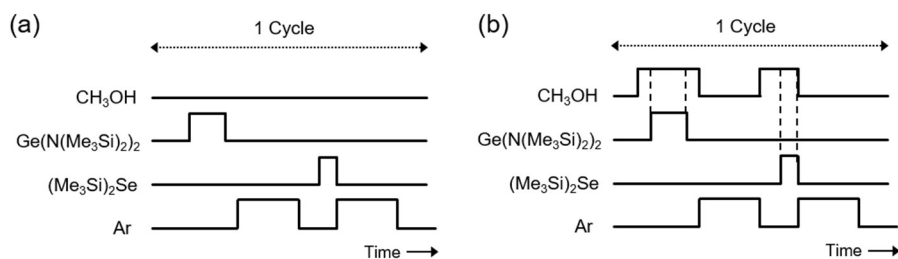
Figure 3-2. Injection sequence of an (a) Typical ALD, without methanol co-injection (b) Modified ALD with methanol co-injection.
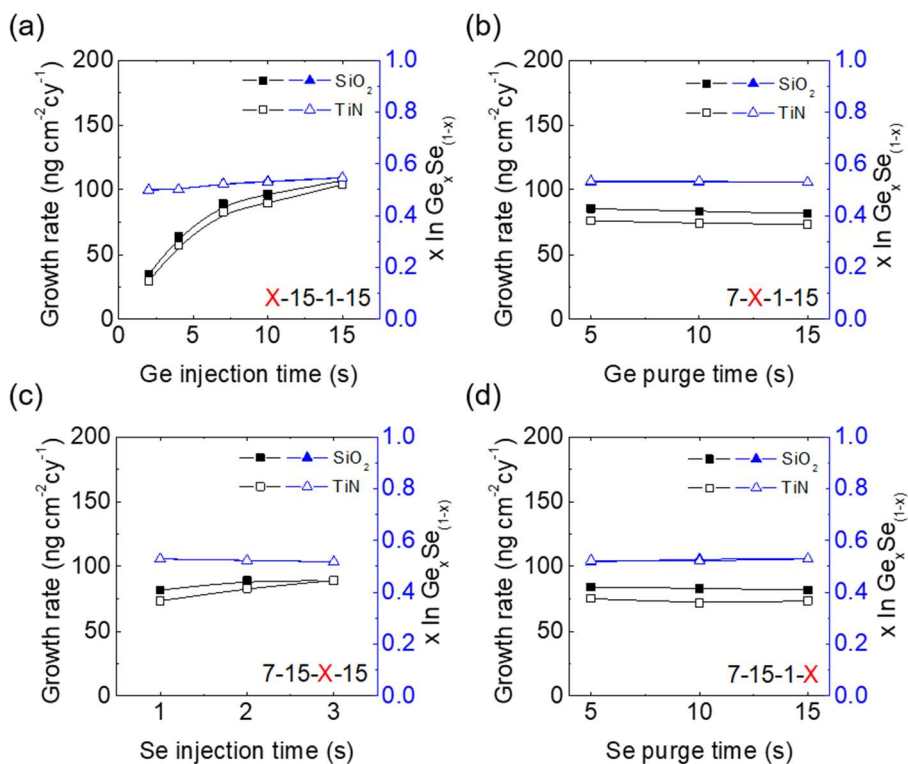
Figure 3-3. Variation in the growth rate and composition of the films grown at 70 °C as a function of (a) Ge precursor injection time (b) Ge precursor purge time (c) Se precursor injection time (d) Se precursor purge time.

surface passivation of the Ge-precursor and can convert the bulky and less reactive -N(Si(CH$_3$)$_3$)$_2$ to compact and more reactive -OCH$_3$ ligand. The following reactions (1)–(3) propose a plausible mechanism to form the intermediate products, Ge(OCH$_3$)$_2$ and H$_2$Se, during GeSe deposition.

$$Ge(N(Si(CH_3)_3)_2)_2 + 6CH_3OH \rightarrow Ge(OCH_3)_2 + 2NH_3 + 4CH_3OSi(CH_3)_3 \tag{1}$$

$$((CH_3)_3Si)_2Se + 2CH_3OH \rightarrow H_2Se + 2CH_3OSi(CH_3)_3 \tag{2}$$

$$Ge(OCH_3)_2 + H_2Se \rightarrow GeSe + 2CH_3OH \tag{3}$$
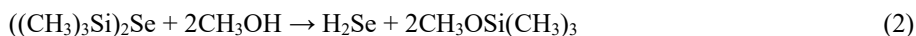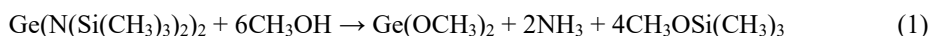
Figure 3-3 shows the growth rate of the GeSe layers on SiO$_2$ and TiN substrates at 70 °C as a function of the Ge- and Se- precursor injection and Ar purge times. The injection sequence follows a modified version that injects methanol 3s before the precursor injection and maintains the methanol flow 5s longer than the precursor injection before subsequent purging begins. The injection and purge times are indicated in seconds at the bottom-right corner of each graph in the order of 'Ge precursor with methanol –Ar purge –Se with methanol – Ar purge times' where 'X' represents the variable in each graph. Figures 3-3 (b)–(d) clearly indicate the saturation behavior of the growing film. Figures 3-3 (b)-(d) show that the growth rates and compositions remain constant at ~80 ng·cm^{-2}·cy^{-1} and Ge:Se=1:1 regardless of the precursor injection and purge time, which is consistent with the stoichiometry of the GeSe produced by Reaction (3). Figure 3-3 (a), however, shows that the growth rate and Ge composition increase continuously with the Ge injection time, similar
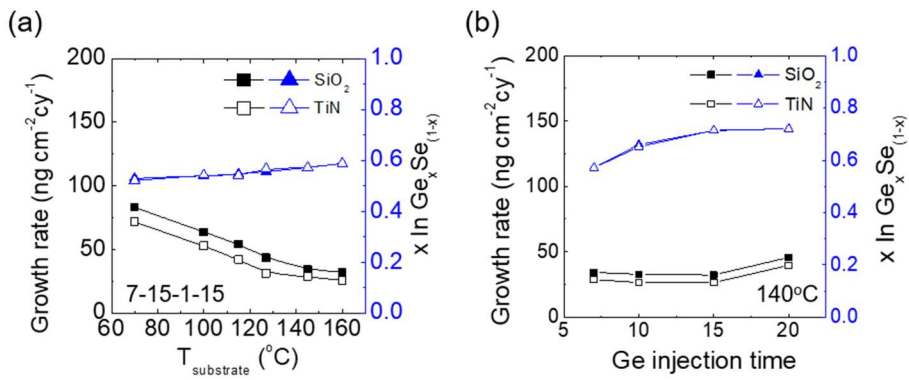
Figure 3-4. Variation in the growth rate and composition of the Ge_xSe_{1-x} films as a function of (a) the growth substrate temperature (b) the Ge injection time at a substrate temperature of 140 ºC.
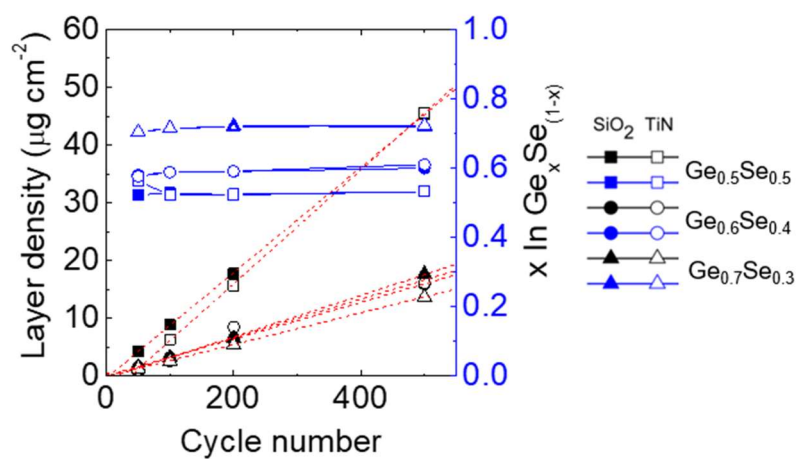
Figure 3-5. Variation in the layer density and composition of the films as a function of the cycle number: $Ge_{0.5}Se_{0.5}$, $Ge_{0.6}Se_{0.4}$, and $Ge_{0.7}Se_{0.3}$.

to the previous report on Ge-Te deposition where the formation of the Ge-Ge bonds between various Ge-intermediates, such as germylene, was proposed as a possible mechanism.[33]

Figure 3-4 (a) summarizes the dependence of the growth rate and composition of the Ge_xSe_{1-x} film at a substrate temperature ranging from 70 to 160 °C with a fixed injection time of Ge precursor of 7s. The Ge composition increased slightly with the increase in substrate temperature, and Ge:Se=6:4 was achieved at 140 °C. Moreover, at an elevated temperature of 140 °C, the Ge composition further increased to Ge:Se=7:3 at a Ge precursor injection time of 15s, as shown in Figure 3-4 (b). The increased Ge composition is assumed to be caused by side reactions between the Ge-intermediates, such as $HGe(OCH_3)$ and $HGe(OCH_3)_3$, which can form compounds with Ge-Ge bonds as in $H(OCH_3)Ge=Ge(OCH_3)_2$.[33] The increase in the Ge composition with the substrate temperature and Ge precursor injection time indicates that the Ge-intermediates participate more actively in the reaction at higher temperatures. The variations in the Ge composition depend on the experimental conditions and offer an opportunity to modulate the film composition of Ge_xSe_{1-x} thin films and to test their effect on the film properties, including electrical characteristics.

Figure 3-5 presents the linear growth behaviors of the $Ge_{0.5}Se_{0.5}$ (7s of Ge-precursor injection at 70 °C substrate temperature), $Ge_{0.6}Se_{0.4}$ (7s injection
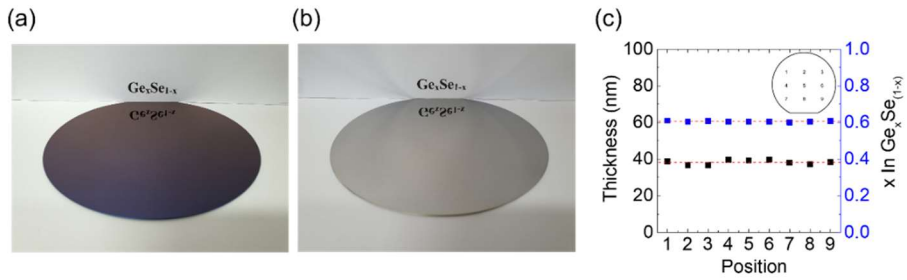
Figure 3-6. Photographic image of (a) a 6 in. Si wafer with 100nm dry oxidized

SiO$_2$. (b) 40 nm thick Ge$_{0.6}$Se$_{0.4}$ (7s of Ge-precursor injection time

at 140 °C, 500 cycles) film deposited on the wafer. (c) Film

thickness (black) and composition (blue) at different locations of

the 6 in. wafer. The local variation in the film thickness and

compositions were ± 4.0 % and 0.8 %, respectively.
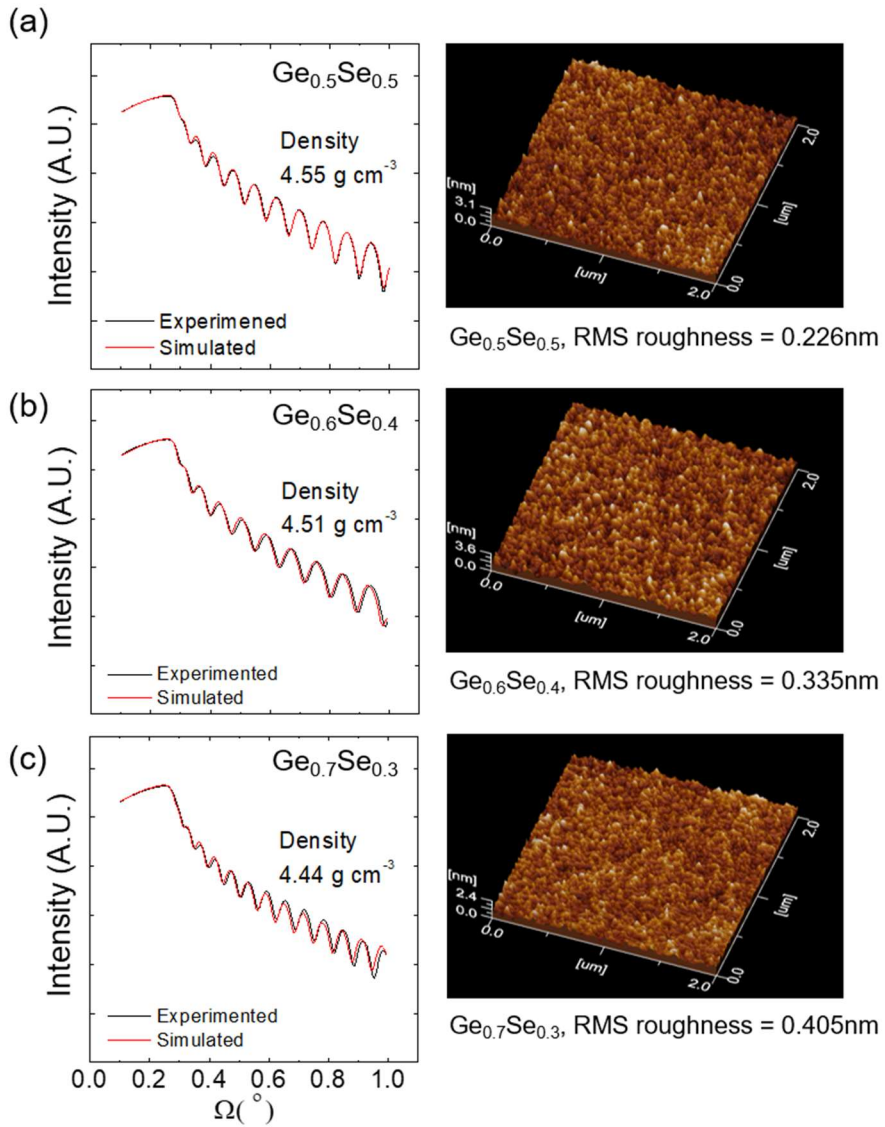
Figure 3-7. XRR and AFM results of (a) $Ge_{0.5}Se_{0.5}$ (b) $Ge_{0.6}Se_{0.4}$ (c) $Ge_{0.7}Se_{0.3}$

films to measure the volume density and surface roughness.

time at 140 ºC), and $Ge_{0.7}Se_{0.3}$ (15s injection time at 140 ºC) films as a function of cycle numbers on SiO_2 and TiN substrates. The growth rates of each composition estimated from the slope of the best linear fitted graph were 91 $ng \cdot cm^{-2} \cdot cy^{-1}$ (2.0 $Å \cdot cy^{-1}$), 32 $ng \cdot cm^{-2} \cdot cy^{-1}$ (0.7 $Å \cdot cy^{-1}$), 35 $ng \cdot cm^{-2} \cdot cy^{-1}$ (0.8 $Å \cdot cy^{-1}$) on the SiO_2 substrate, respectively. The thickness was calculated by dividing the layers' areal density by the volume density of the film measured by XRR. A uniformity test was performed by depositing 40 nm thick $Ge_{0.6}Se_{0.4}$ (7s Ge-precursor injection time at 140 ºC, 500 cycles) film on a 6-inch Si whole wafer. A photo image of the wafer and XRF results by several positions are attached in Figure 3-6. Figure 3-7 summarizes the bulk density and the surface morphologies of the various as-deposited Ge_xSe_{1-x} films, which were 50nm-thick and grown on the SiO_2 substrate. The bulk density of the as-deposited $Ge_{0.5}Se_{0.5}$ film was 4.55 $g \cdot cm^{-3}$, measured by fitting the XRR result assuming a $Ge_{0.5}Se_{0.5}/SiO_2/Si$ laminate film structure, as shown in Figure 3-7 (a). The bulk density of the amorphous GeSe film was 82% compared to the theoretical density of the crystalline GeSe film, 5.56 $g \cdot cm^{-3}$. Considering that the density of the thermally oxidized amorphous SiO_2 is 83% compared to that of the crystallized SiO_2 (amorphous SiO_2: 2.20 $g \cdot cm^{-3}$, crystalline SiO_2: 2.65 $g \cdot cm^{-3}$), the density of the as-deposited amorphous GeSe by ALD can be considered to be sufficiently high. Also, this density value is 10% higher than that of the ALD GeSe observed in the previous report.[31] Since the film density significantly influences the reliability of the electrical characteristic (e.g., void-induced
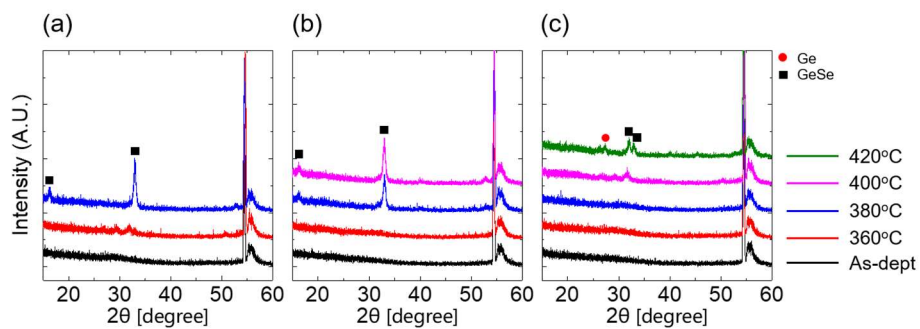
Figure 3-8. Glancing angle X-ray diffraction patterns of as-deposited and annealed (a) $Ge_{0.5}Se_{0.5}$ (b) $Ge_{0.6}Se_{0.4}$ (c) $Ge_{0.7}Se_{0.3}$ films.

failure during OTS cycling), the high-density suggests the strong potential of the deposited film for use in OTS applications. The surface morphology measured using AFM showed an extremely low RMS roughness of 0.226 nm. The low roughness value confirms a fluent ALD reaction on the surface of the substrate from the very beginning of the ALD cycle. The bulk density and the surface morphology of the Ge-rich $Ge_{0.6}Se_{0.4}$ and $Ge_{0.7}Se_{0.3}$ films in Figures 3-7 (b) and (c) are 4.51 g·cm^{-3} with 0.335 nm, and 4.44 g·cm^{-3} with 0.405 nm, which did not differ significantly from those of the $Ge_{0.5}Se_{0.5}$ film.

Figure 3-8 shows the glancing angle X-ray diffraction (GAXRD) patterns of the as-deposited (~50nm-thick) and annealed Ge-Se film to confirm its crystallization temperature. The annealing process was held in a furnace under ambient air condition for 30 minutes. The $Ge_{0.5}Se_{0.5}$ film was deposited as amorphous and was crystallized at a temperature of 380 ℃, which corresponds well to the crystallization temperature of the bulk Ge-Se. With a higher Ge composition, the film crystallized at higher temperatures, which is advantageous for an OTS-based selector due to the increased amorphous stability. However, if the composition of the Ge was too high ($Ge_{0.7}Se_{0.3}$), Ge segregation occurred, as indicated by the red dot in the $Ge_{0.7}Se_{0.3}$ composition result, which may cause a negative effect on the OTS behavior.
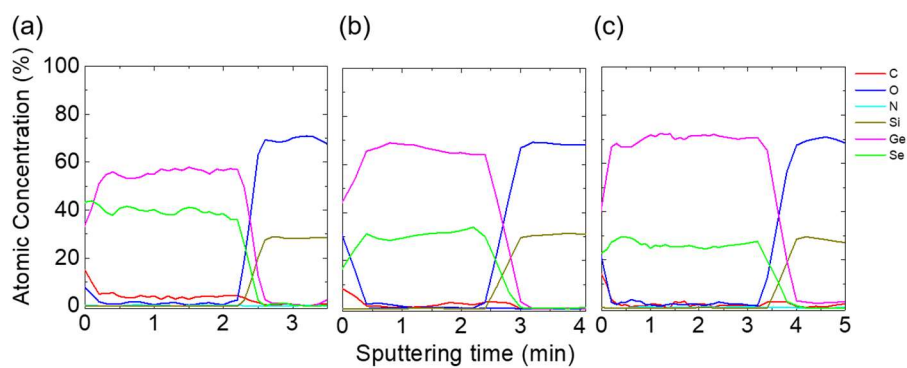
Figure 3-9. Auger electron spectroscopy of Ge_xSe_{1-x} films. Analyzed atoms are

C, N, O, Si, Ge, and Se (a) $Ge_{0.5}Se_{0.5}$ (b) $Ge_{0.6}Se_{0.4}$ (c) $Ge_{0.7}Se_{0.3}$.
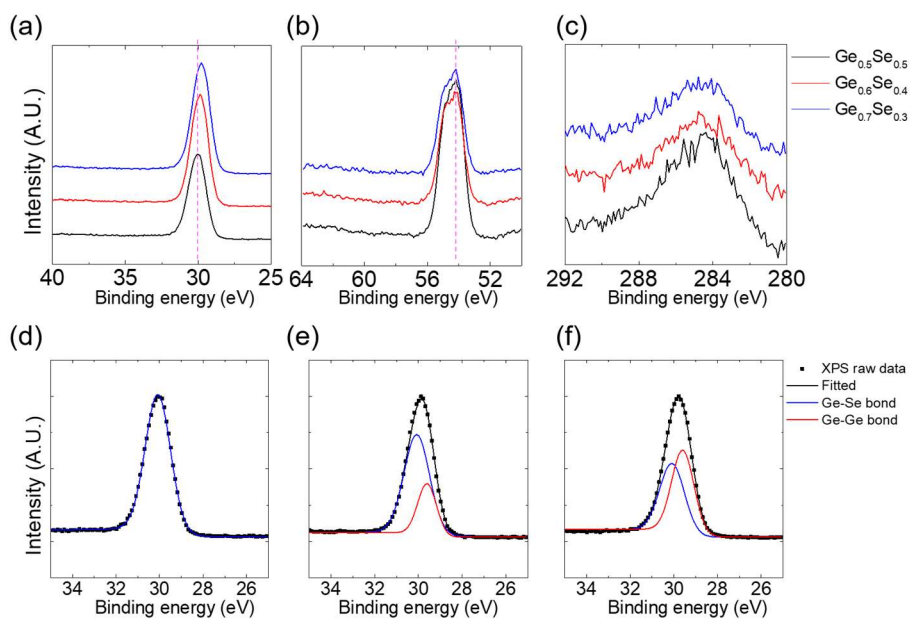
Figure 3-10. (a) Ge 3*d*, (b) Se 3*d*, and (c) C 1*s* XPS spectra of the as-deposited

Ge_xSe_{1-x} films. Curved-fitted Ge 3d XPS spectrum of (d) $Ge_{0.5}Se_{0.5}$,

(e) $Ge_{0.6}Se_{0.4}$, and (f) $Ge_{0.7}Se_{0.3}$ films. The area ratio of Ge-Se : Ge-

Ge bond is (d) 100 : 0, (e) 2.15 : 1, and (f) 3.3 : 4.

The depth-profiling AES result in Figure 3-9 reveals that the film compositions are uniform across the entire film thickness and confirmed a low level of nitrogen, oxygen, and silicon impurities in the entire Ge_xSe_{1-x} film. Only relative variations are meaningful in the AES results due to the absence of an appropriate reference. It should be noted that the carbon impurity of the $Ge_{0.5}Se_{0.5}$ film was significant, at up to 5%, which is known to lower the threshold voltage of GeSe.[34] The carbon impurity decreased slightly for the $Ge_{0.6}Se_{0.4}$ and $Ge_{0.7}Se_{0.3}$ films, which were deposited at higher substrate temperatures. The carbon impurity in the $Ge_{0.5}Se_{0.5}$ film can be caused by the physisorption of carbon by complex intermediates derived from methanol co-injection.

XPS was used to validate the chemical states of the Ge_xSe_{1-x} films. Figure 3-10 (a)–(c) shows Ge $3d$, Se $3d$, and C $1s$ XPS spectra of the as-deposited Ge_xSe_{1-x} films, which were cleaned by Ar^+ ion sputtering to remove the native oxide layer. The Ge $3d$ peak of the $Ge_{0.5}Se_{0.5}$ film was centered at 30.1 eV, which corresponds to the Ge-Se binding energy.[35, 36] The Ge-rich Ge_xSe_{1-x} film peaks have lower binding energy due to the low binding energy of the Ge-Ge bond. Consequently, the binding energy of $Ge_{0.6}Se_{0.4}$ and $Ge_{0.7}Se_{0.3}$ films slightly shifted to 29.9 and 29.8 eV, respectively. Each peak was fitted to the Ge-Se (30.1 eV) and Ge-Ge (29.6 eV) bond, and the ratio of Ge-Se to Ge-Ge bonds changed, suiting the Ge_xSe_{1-x} composition. Detailed fitting results are in Figure 3-10 (d)–(f). On the other hand, the chemical environment of the Se
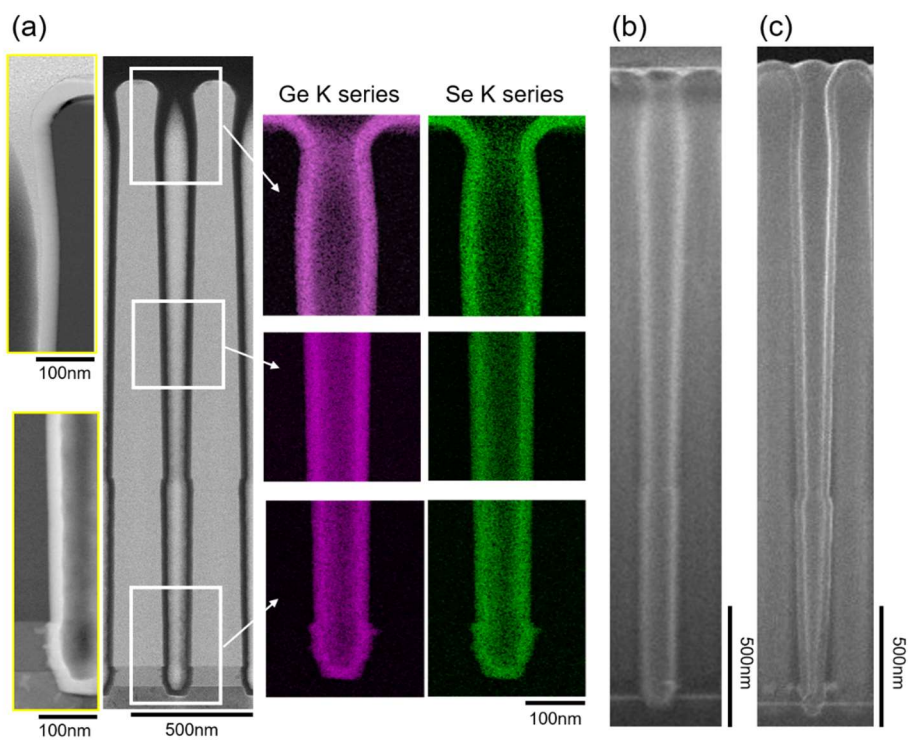
Figure 3-11. (a) Cross-section TEM and EDS composition mapping results $Ge_{0.5}Se_{0.5}$, and cross-section SEM images of (b) $Ge_{0.6}Se_{0.4}$ and (c) $Ge_{0.7}Se_{0.3}$ showing conformal deposition of the films grown on a contact hole structure.

atoms remained invariant at the same binding energy of 54.2 eV, which corresponds to the Se-Ge binding energy, as shown in the Se $3d$ spectra in Figure 3-10 (b). The Ge-rich composition of the deposited Ge_xSe_{1-x} thin film results from the reaction between Ge intermediates, as mentioned above, without any participation of the Se precursor. As can be seen in the C $1s$ spectra of Figure 3-10 (c), the carbon peak intensity was slightly higher at the $Ge_{0.5}Se_{0.5}$, which is deposited at a relatively low temperature of 70 °C. This corroborates with the AES data in Figure 3-9.

The step coverage of the ALD Ge_xSe_{1-x} film is confirmed by obtaining cross-sectional TEM and SEM images. Figure 3-11 (a) shows the TEM images and EDS composition mapping images of the $Ge_{0.5}Se_{0.5}$ layer grown on a contact hole structure. The opening diameter of the contact hole structure is 120 nm with a hole depth of 2500 nm, giving an aspect ratio of 1:20. Even for such an extreme geometry, a completely uniform thickness was obtained with the chemical composition covering the entire surface. Both the $Ge_{0.6}Se_{0.4}$ and $Ge_{0.7}Se_{0.3}$ films also exhibited a completely uniform thickness over the extreme geometry, as shown in the SEM image of Figures 3-11 (b) and (c). Film conformality in a high- aspect-ratio contact hole is critically important to fabricate a 3D vertical memory array for ultrahigh density applications. The ultimate conformal deposition of this ALD process reveals the feasibility of using the Ge-Se film as a selector element for the 3D vertical memory.
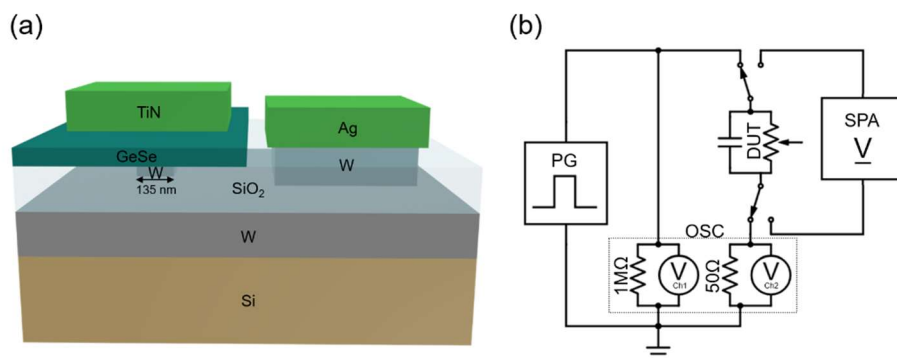
Figure 3-12. Experimental set-up for the OTS measurement. (a) Schematic diagram of the OTS device structure fabricated on a W-plug-patterned substrate with a contact diameter of 135 nm (b) PG and SMU measurement system.
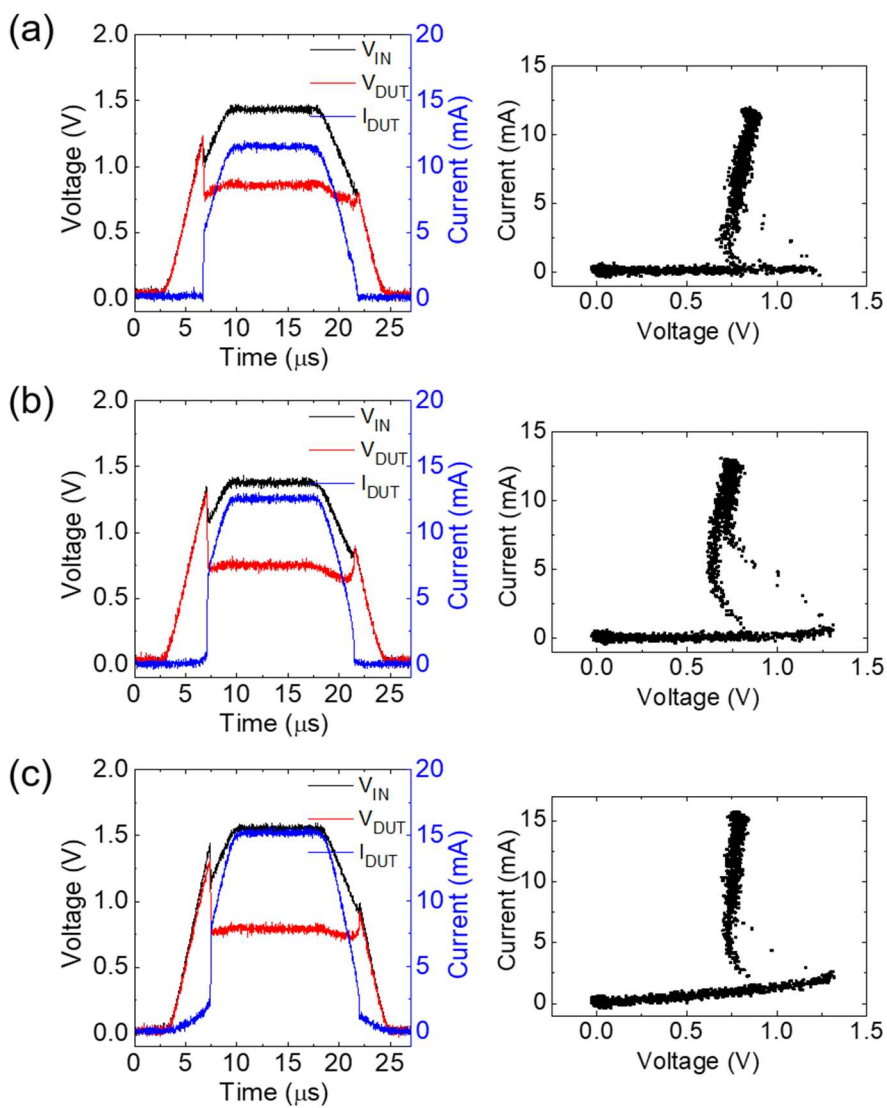
Figure 3-13. Representative pulse response of the Ge_xSe_{1-x} films and its conversion to current-voltage curves. (a) $Ge_{0.5}Se_{0.5}$, (b) $Ge_{0.6}Se_{0.4}$, and (c) $Ge_{0.7}Se_{0.3}$.

A mushroom-type cell was fabricated to evaluate the electrical characteristics of the Ge_xSe_{1-x} films. Figure 3-12 shows the device structure and the circuit that was used to measure the OTS behavior. The Ge_xSe_{1-x} films were deposited on a W-plug-patterned substrate, and electric pulses were applied through the TiN and Ag electrodes, as shown in Figure 3-12 (a). The circuit used to measure the pulse response and voltage sweep is shown in Figure 3-12 (b). The difference between the reference voltage of channel 1 (V_{Ch1}) and channel 2 (V_{Ch2}) corresponds to the voltage applied to the device under test (V_{DUT}). The PG generates a trapezoidal pulse, and an OSC was used to observe the device response of the 'ON state.' The SPA measured the 'OFF state' current due to the limited precision of the OSC in measuring a low current. The 'OFF state' resistance was calculated by reading the current at a voltage of 0.7 V, which is approximately half of the threshold voltage. The OTS measurement results of the devices fabricated with each of the Ge_xSe_{1-x} compositions are shown in Figure 3-13. Figure 3-13 shows a representative response of devices to a long trapezoidal pulse, which was taken after applying 1000 pulses. All device tests were performed after a first fire operation which applied a 3 V pulse for 500 ns with a serially connected 2.2 kΩ resistor as a current limiter to minimize the structural change of the Ge_xSe_{1-x} film. Once the applied voltage exceeds the threshold voltage (V_{th}, here 1.2 to 1.5 V), switching occurs rapidly from an initial high resistance 'OFF state' into a highly conductive dynamic 'ON state.' The sudden decrease in V_{IN} and V_{DUT}, which is called the 'voltage

snapback,' can be observed in the dynamic switching at V_{th}. This can be more prominently seen from the I_{DUT}-V_{DUT} curve depicted in the right graph of Figure 3-13. After its low resistance in the 'ON state,' the device volatilely switches back into the 'OFF state' when the applied voltage drops below the holding voltage (V_h).

The most notable feature of the present Ge_xSe_{1-x} thin film is the considerably low V_{th} compared to other Ge_xSe_{1-x} films deposited by a sputtering technique that was presented in previous studies.[8,37] The V_{th} slightly increased with faster voltage ramp, but still remained at a low level (V_{th}=1.6 V for $Ge_{0.6}Se_{0.4}$ with a voltage pulse with 20 ns rise / 500 ns plateau / 20 ns fall times). Typically, the V_{th} of the sputtered Ge_xSe_{1-x} ranges from 3 to 7 V.[8,37] The low threshold voltage is important to operate the 1S-1R device because the selector should switch to the ON state below the writing voltage of the resistor. For this reason, the modulation of the V_{th} of the OTS devices was attempted for the stable switching in the 1S-1R device. Dopants such as C, Bi, Sb are adopted to achieve a lower V_{th} for a higher read/write voltage margin.[12,34,38] Previous studies reported that carbon doping via sputtering lowered the V_{th} of GeSe from 3.0 V to 1.5 V because the doped carbon played the role as an electronic trap state by forming triple coordinated $C-Ge_3$ although the detailed compositions were not unveiled.[34,39] As seen from the AES result of the present work, shown in Figures 3-9, a small amount of carbon impurity was present in the Ge_xSe_{1-x} film. Any other impurities such as nitrogen, oxygen, and silicon which were
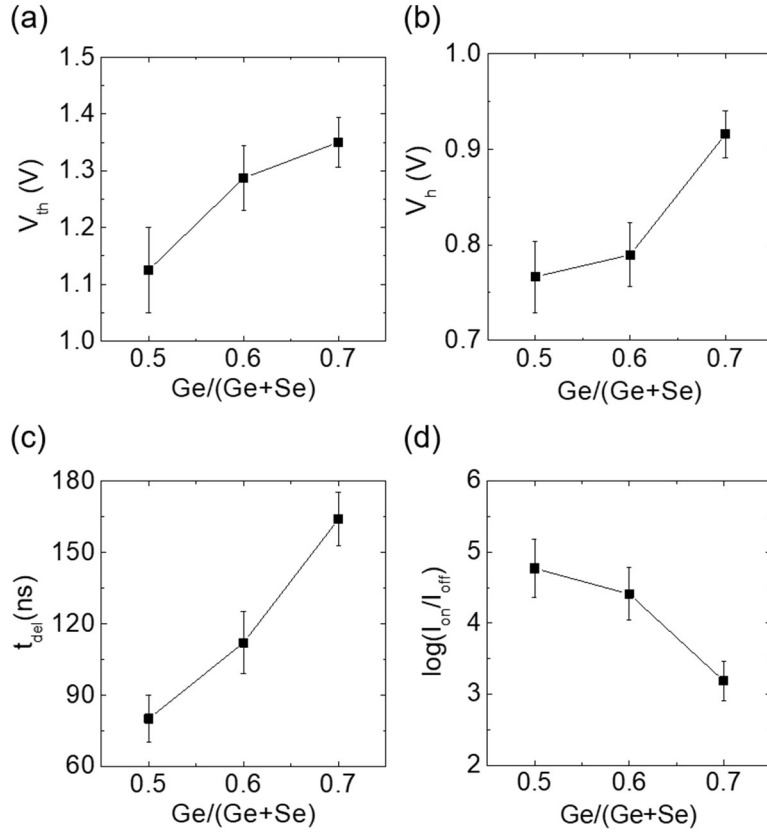
Figure 3-14. (a) The threshold voltage (V_{th}), (b) holding voltage (V_h), (c) delay time (t_{del}), and (d) selectivity (I_{on}/I_{off}) of the investigated devices as a function of the Ge concentration.
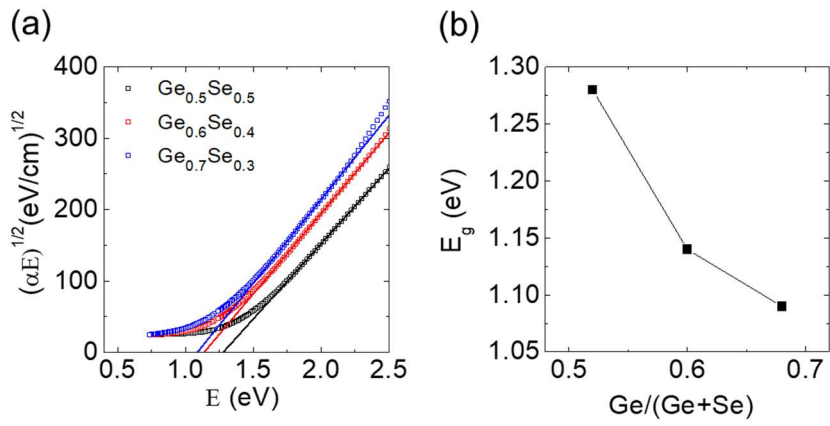
Figure 3-15. (a) Spectroscopic ellipsometry and the Tauc plot of each film. (b)

The extracted bandgap (E_g) for different films.

contained in the ALD precursors were negligible. Impurities were cross-checked by XPS spectra, as shown in Figures 3-10 (c), and only the peak of carbon 1s was shown. This carbon impurity possibly resulted from a complex reaction between the various intermediate precursors from the reaction with co-injected methanol. Considering that carbon was the only impurity in the ALD Ge_xSe_{1-x} film and the V_{th} was similar to the previous studies, it was confirmed that the low V_{th} of the present ALD Ge_xSe_{1-x} film could be attributed to the carbon doping effect.

The variations in the V_{th}, V_h, delay time (t_{del}), and selectivity (I_{on}/I_{off}) of the investigated devices are summarized in Figure 3-14 as a function of the Ge concentration. Here, t_{del} is estimated as the time required to induce a sudden increase in the I_{DUT} shown in the left panels of Figures 3-13 (a), (b), and (c). The error bars represent measurement errors of a single device. The V_{th} increases with Ge contents, which is contrast to the measured bandgap shown in Figure 3-15. It has been reported that the V_{th} decreased with the decreasing bandgap of Ge_xSe_{1-x} films.[9,37] Such an inconsistency with the previous reports can be understood by the difference in the carbon impurity level, which has been known to lower V_{th}.[34,39] The present ALD process uses higher temperatures for the deposition of Ge-rich films, which produces a lower concentration of carbon impurity. The $Ge_{0.5}Se_{0.5}$ film can be understood to have the most promising performance for all device parameters, which could be ascribed ascribed to the appropriate involvement of carbon impurities. However,
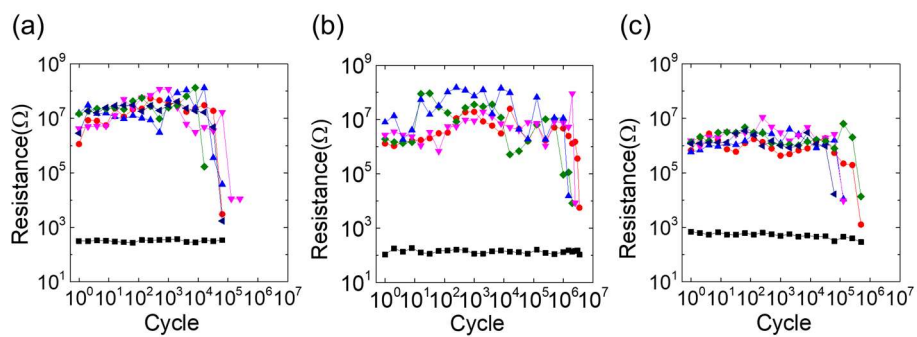
Figure 3-16. Cycling endurance of (a) $Ge_{0.5}Se_{0.5}$, (b) $Ge_{0.6}Se_{0.4}$ and (c) $Ge_{0.7}Se_{0.3}$.

as shown below, its relatively low endurance is a problem.

Figure 3-16 shows the cycle endurance of the Ge_xSe_{1-x} devices. The cyclic endurance was obtained by applying repetitive high-voltage pulses, and low-voltage I-V sweeps, alternatively. The high-voltage pulse was set to 3 V (1 μs rise, 1 μs plateau, and 1 μs fall time) to read the 'ON state' resistance, and the 'OFF state' resistance was calculated by reading the current at a voltage of 0.7 V using the SPA. A serially connected external resistance of 2.2 kΩ was attached as a current limiter to reduce the ON current. An endurance of over 10^5 was obtained with a half-bias nonlinearity of 10^5 for $Ge_{0.5}Se_{0.5}$ in Figure 3-16 (a). These data show that the ALD $Ge_{0.5}Se_{0.5}$ selector can deliver high drive currents, enabling 1S-1R with large write currents while having good selectivity and reliability to prevent a misleading sneak current. The OTS behavior showed an 'ON state' stuck failure, inferring the failure occurred with the crystallization of the GeSe resulting from Joule heating. The selectivity and endurance of the $Ge_{0.6}Se_{0.4}$ and $Ge_{0.7}Se_{0.3}$ films are shown in Figures 3-16 (b) and (c), respectively. Comparing the measured performance of the OTS, the OFF resistance was lower, and the selectivity was slightly degraded in these Ge-rich films. This is due to the smaller bandgap of the amorphous Ge itself of ~0.6 eV, which may induce local leakage current path formation in the OFF state. Also, the bandgap of each composition was confirmed by the Tauc plot, using a SE as in Figure 3-15 (1.28 eV for $Ge_{0.5}Se_{0.5}$, 1.14 eV for $Ge_{0.6}Se_{0.4}$, and 1.09 eV for $Ge_{0.7}Se_{0.3}$). Therefore, the lower bandgap of the Ge-rich material also

contributed to a higher leakage current. The cycle endurance results show that the operation endurance of the $Ge_{0.6}Se_{0.4}$ film was the highest, which shows over 10^6 cycles with over 10^4 half-bias nonlinearity.

It should also be noted that the deposition temperature of the 6:4 composition (140 °C) is the most compatible with recently reported ALD of crystalline-as-deposited $Ge_2Sb_2Te_5$ when forming a 1S-1R stack.[29] A previous report on the $Ge_2Sb_2Te_5$ ALD showed that a low deposition temperature (below 110 °C) resulted in low-density and high-impurity films, while a too high deposition temperature (over ~150 °C) increased the high roughness of the films due to the larger grain size.

3.4. Conclusion

In conclusion, Ge-Se films can be deposited by utilizing the self-limiting behavior of the ALD process with $Ge(N(Si(CH_3)_3)_2)_2$ and $((CH_3)_3Si)_2Se$ precursors and methanol co-injection at a low temperature ranging from 70 to 160 °C. The as-deposited Ge-Se film was amorphous with a low film roughness, high density, and most importantly, excellent conformality. The completely uniform thickness over the extreme geometry revealed its suitability for use in three-dimensional vertical memory applications. A demonstration was carried out with OTS devices of the deposited Ge-Se by fabricating a mushroom-type cell with a contact diameter of 135 nm. The device achieved a half-bias nonlinearity of 10^5 and 10^5 cycle endurance when using the $Ge_{0.5}Se_{0.5}$ film. Notably, the low threshold voltage of 1.2 V could be achieved, which must be a critical ingredient to integrate the OTS with the resistance-based nonvolatile memory materials.

The process temperature and Ge precursor injection time were varied to enable the formation of Ge-Se films with different contents of Ge_xSe_{1-x} (x=0.5 to 0.7). Specifically, the Ge composition increased with a higher deposition temperature and a longer Ge precursor injection time. The additional Ge-rich composition of the deposited Ge_xSe_{1-x} thin film was due to the reaction between the Ge intermediates, such as $HGe(OCH_3)$ and $HGe(OCH_3)_3$. The OTS device with the $Ge_{0.6}Se_{0.4}$ film achieved a half-bias nonlinearity of 10^4 and 10^6 cycle

endurance, which is the highest among the reported chalcogenide-based OTS selectors deposited by ALD. This work presents the foundations for the future development of ultra-high capacity vertical-type 1S-1R arrays combined with the authors' ALD $Ge_2Sb_2Te_5$.[29]

3.5. References

(1)   Jeong, D. S.; Thomas, R.; Katiyar, R. S.; Scott, J. F.; Kohlstedt, H.; Petraru, A.; Hwang, C. S. Emerging Memories: Resistive Switching Mechanisms and Current Status. Reports Prog. Phys. 2012, 75 (7), 076502.

(2)   Lankhorst, M. H. R.; Ketelaars, B. W. S. M. M.; Wolters, R. A. M. Low-Cost and Nanoscale Non-Volatile Memory Concept for Future Silicon Chips. Nat. Mater. 2005, 4 (4), 347–352.

(3)   Chen, A. A Review of Emerging Non-Volatile Memory (NVM) Technologies and Applications. Solid. State. Electron. 2016, 125, 25–38.

(4)   Yoon, K. J.; Kim, Y.; Hwang, C. S. What Will Come After V-NAND — Vertical Resistive Switching Memory? Adv. Electron. Mater. 2019, 1800914, 1–15.

(5)   Burr, G. W.; Shenoy, R. S.; Virwani, K.; Narayanan, P.; Padilla, A.; Kurdi, B.; Hwang, H. Access Devices for 3D Crosspoint Memory. *J. Vac. Sci. Technol. B, Nanotechnol. Microelectron. Mater. Process. Meas. Phenom.* **2014**, *32* (4), 040802.

(6)   Shanks, R. R. Ovonic Threshold Switching Characteristics. *J. Non. Cryst. Solids* **1970**, *2* (C), 504–514.

(7)   Czubatyj, W.; Hudgens, S. J. Thin-Film Ovonic Threshold Switch: Its Operation and Application in Modern Integrated Circuits. *Electron. Mater. Lett.* **2012**, *8* (2), 157–167.

(8)   Ahn, H. W.; Jeong, D. S.; Cheong, B. K.; Kim, S. D.; Shin, S. Y.; Lim, H.; Kim, D.; Lee, S. A Study on the Scalability of a Selector Device Using Threshold Switching in Pt/GeSe/Pt. *ECS Solid State Lett.* **2013**, *2* (9), 2013–2016.

(9)   Avasarala, N. S.; Donadio, G. L.; Witters, T.; Opsomer, K.; Govoreanu, B.;

Fantini, A.; Clima, S.; Oh, H.; Kundu, S.; Devulder, W.; van der Veen, M. H.; Van Houdt, J.; Heyns, M.; Goux, L.; Kar, G.S. Half-Threshold Bias I_{off} Reduction down to NA Range of Thermally and Electrically Stable High-Performance Integrated OTS Selector, Obtained by Se Enrichment and N-Doping of Thin GeSe Layers. *Dig. Tech. Pap. - Symp. VLSI Technol.* **2018**, *2018-June* (4), 209–210.

(10)   Liu, G.; Wu, L.; Chen, X.; Li, T.; Wang, Y.; Guo, T. The Investigations of Characteristics of GeSe Thin Films and Selector Devices for Phase Change Memory. *J. Alloys Compd.* **2019**, *792*, 510–518.

(11)   Chai, Z.; Zhang, W.; Degraeve, R.; Clima, S.; Hatem, F.; Zhang, J. F.; Freitas, P.; Marsland, J.; Fantini, A.; Garbin, D.; Goux, L.; Kar, G.S. Dependence of Switching Probability on Operation Conditions in Ge_xSe_{1-x} Ovonic Threshold Switching Selectors. *IEEE Electron Device Lett.* **2019**, *40* (8), 1269–1272.

(12)   Seo, J.; Ahn, H. W.; Shin, S. Y.; Cheong, B. K.; Lee, S. Anomalous Reduction of the Switching Voltage of Bi-Doped $Ge_{0.5}Se_{0.5}$ Ovonic Threshold Switching Devices. *Appl. Phys. Lett.* **2014**, *104* (15), 0–4.

(13)   Shin, S. Y.; Choi, J. M.; Seo, J.; Ahn, H. W.; Choi, Y. G.; Cheong, B. K.; Lee, S. The Effect of Doping Sb on the Electronic Structure and the Device Characteristics of Ovonic Threshold Switches Based on Ge-Se. *Sci. Rep.* **2014**, *4*, 4–8.

(14)   Navarro, G.; Verdy, A.; Castellani, N.; Bourgeois, G.; Sousa, V.; Molas, G.; Bernard, M.; Sabbione, C.; Noe, P.; Garrione, J.; Fellouh, L.; Perniola, L. Innovative PCM+OTS Device with High Sub-Threshold Non-Linearity for Non-Switching Reading Operations and Higher Endurance Performance. *Dig. Tech. Pap. - Symp. VLSI Technol.* **2017**, *2* (10), T94–T95.

(15)   Alayan, M.; Vianello, E.; Navarro, G.; Carabasse, C.; La Barbera, S.; Verdy, A.;

Castellani, N.; Levisse, A.; Molas, G.; Grenouillet, L.; Magis, T.; Aussenac, F.; Bernard, M.; DeSalvo, B.; Portal, J.M.; Nowak, E. In-Depth Investigation of Programming and Reading Operations in RRAM Cells Integrated with Ovonic Threshold Switching (OTS) Selectors. *Tech. Dig. - Int. Electron Devices Meet. IEDM* **2018**, No. 1, 2.3.1-2.3.4.

(16) Woo, J.; Yu, S. Device Design and Material Considerations of Ovonic Threshold Switch (OTS) for Cross-Point MRAM Array. *2019 Electron Devices Technol. Manuf. Conf. EDTM* **2019**, No. 1, 148–150.

(17) Luo, Q.; Xu, X.; Gong, T.; Lv, H.; Dong, D.; Ma, H.; Yuan, P.; Gao, J.; Liu, J.; Yu, Z.; Li, J.; Long, S.; Liu, Q.; Liu, M. 8-Layers 3D Vertical RRAM with Excellent Scalability towards Storage Class Memory Applications. *Tech. Dig. - Int. Electron Devices Meet. IEDM* **2018**, *2*, 2.7.1-2.7.4.

(18) Hady, F. T.; Foong, A.; Veal, B.; Williams, D. Platform Storage Performance with 3D XPoint Technology. *Proc. IEEE* **2017**, *105* (9), 1822–1833.

(19) Qin, S.; Jiang, Z.; Li, H.; Fujii, S.; Lee, D.; Simon Wong, S.; Wong, H. S. P. Next-Generation Ultrahigh-Density 3-D Vertical Resistive Switching Memory (VRSM)-Part I: Accurate and Computationally Efficient Modeling. *IEEE Trans. Electron Devices* **2019**, *66* (12), 5139–5146.

(20) Jiang, Z.; Qin, S.; Li, H.; Fujii, S.; Lee, D.; Wong, S.; Philip Wong, H. S. P. Next-Generation Ultrahigh-Density 3-D Vertical Resistive Switching Memory (VRSM)-Part II: Design Guidelines for Device, Array, and Architecture. *IEEE Trans. Electron Devices* **2019**, *66* (12), 5147–5154.

(21) M, G. S. Atomic Layer Deposition: An Overview. *Chem. Rev.* **2010**, *110*, 111.

(22) Gordon, R. G. ALD Precursors and Reaction Mechanisms. *At. Layer Depos. Semicond.* **2014**, *9781461480*, 15–46.

(23)   Hwang, C. J. ALD(Atomic Layer Deposition) Process Technology in the Semiconductor Industry. *Phys. High Technol.* **2012**, *21* (1/2), 37.

(24)   Park, E. S.; Yoo, C.; Kim, W.; Ha, M.; Jeon, J. W.; Lee, Y. K.; Hwang, C. S. Developing Precursor Chemistry for Atomic Layer Deposition of High-Density, Conformal GeTe Films for Phase-Change Memory. *Chem. Mater.* **2019**, *31* (21), 8663-8672.

(25)   Eom, T.; Choi, S.; Choi, B. J.; Lee, M. H.; Gwon, T.; Rha, S. H.; Lee, W.; Kim, M. S.; Xiao, M.; Buchanan, I.; Cho, D. Y.; Hwang, C. S. Conformal Formation of $(GeTe_2)_{(1-x)}(Sb_2Te_3)_x$ Layers by Atomic Layer Deposition for Nanoscale Phase Change Memories. *Chem. Mater.* **2012**, *24* (11), 2099–2110.

(26)   Eom, T.; Gwon, T.; Yoo, S.; Choi, B. J.; Kim, M. S.; Buchanan, I.; Ivanov, S.; Xiao, M.; Hwang, C. S. Combined Ligand Exchange and Substitution Reactions in Atomic Layer Deposition of Conformal $Ge_2Sb_2Te_5$ Film for Phase Change Memory Application. *Chem. Mater.* **2015**, *27* (10), 3707–3713.

(27)   Eom, T.; Gwon, T.; Yoo, S.; Choi, B. J.; Kim, M.-S.; Ivanov, S.; Adamczyk, A.; Buchanan, I.; Xiao, M.; Hwang, C. S. Chemical Interaction and Ligand Exchange between a $[(CH_3)_3Si]_3Sb$ Precursor and Atomic Layer Deposited Sb_2Te_3 Films. *J. Mater. Chem. C* **2015**, *3* (6), 1365–1370.

(28)   Gwon, T.; Eom, T.; Yoo, S.; Yoo, C.; Park, E. S.; Kim, S.; Kim, M. S.; Buchanan, I.; Xiao, M.; Ivanov, S.; Hwang, C. S. Atomic Layer Deposition of GeTe and Ge-Sb-Te Films Using $HGeCl_3$, $Sb(OC_2H_5)_3$, and $\{(CH_3)_3Si\}_2Te$ and Their Reaction Mechanisms. *Chem. Mater.* **2017**, *29* (19), 8065–8072.

(29)   Park, E. S.; Yoo, C.; Kim, W.; Ha, M.; Jeon, J. W.; Eom, T.; Lee, Y. K.; Hwang, C. S. Atomic Layer Deposition of Nanocrystalline-As-Deposited $(GeTe)_x(Sb_2Te_3)_{1-x}$ Films for Endurable Phase Change Memory. *Chem. Mater.* **2019**, *31* (21), 8752-8763.

(30) Ritala, M.; Pore, V.; Hatanpää, T.; Heikkilä, M.; Leskelä, M.; Mizohata, K.; Schrott, A.; Raoux, S.; Rossnagel, S. M. Atomic Layer Deposition of $Ge_2Sb_2Te_5$ Thin Films. *Microelectron. Eng.* **2009**, *86* (7–9), 1946–1949.

(31) Kim, W.; Yoo, S.; Yoo, C.; Park, E. S.; Jeon, J.; Kwon, Y. J.; Woo, K. S.; Kim, H. J.; Lee, Y. K.; Hwang, C. S. Atomic Layer Deposition of GeSe Films Using $HGeCl_3$ and $[(CH_3)_3Si]_2Se$ with the Discrete Feeding Method for the Ovonic Threshold Switch. *Nanotechnology* **2018**, *29* (36), 365202.

(32) Yoo, S.; Yoo, C.; Park, E. S.; Kim, W.; Lee, Y. K.; Hwang, C. S. Chemical Interactions in the Atomic Layer Deposition of Ge-Sb-Se-Te Films and Their Ovonic Threshold Switching Behavior. *J. Mater. Chem. C* **2018**, *6* (18), 5025–5032.

(33) Gwon, T.; Eom, T.; Yoo, S.; Lee, H. K.; Cho, D. Y.; Kim, M. S.; Buchanan, I.; Xiao, M.; Ivanov, S.; Hwang, C. S. Atomic Layer Deposition of GeTe Films Using $Ge\{N[Si(CH_3)_3]_2\}_2$, $\{(CH_3)_3Si\}_2Te$, and Methanol. *Chem. Mater.* **2016**, *28* (19), 7158–7166.

(34) Avasarala, N. S.; Govoreanu, B.; Opsomer, K.; Devulder, W.; Clima, S.; Detavernier, C.; Van Der Veen, M.; Van Houdt, J.; Henys, M.; Goux, L.; Kar, G. S. Doped GeSe Materials for Selector Applications. *Eur. Solid-State Device Res. Conf.* **2017**, 168–171.

(35) Ueno, T. X-ray Photoelectron and Auger Electron Spectroscopic Studies of Chemical Shifts in Amorphous Ge-Se System. *Japanese J. Appl. Physics, Part 1 Regul. Pap. Short Notes* **1983**, *22* (9), 1349–1352.

(36) Rumble, J. R.; Bickham, D. M.; Powell, C. J. The NIST X-ray Photoelectron Spectroscopy Database. *Surf. Interface Anal.* **1992**, *19* (1–12), 241–246.

(37) Kim, S.-D.; Ahn, H.-W.; Shin, S. y.; Jeong, D. S.; Son, S. H.; Lee, H.; Cheong,

B. -k.; Shin, D. W.; Lee, S. Effect of Ge Concentration in Ge_xSe_{1-x} Chalcogenide Glass on the Electronic Structures and the Characteristics of Ovonic Threshold Switching (OTS) Devices. *ECS Solid State Lett.* **2013**, *2* (10), Q75–Q77.

(38)   Verdy, A.; Navarro, G.; Sousa, V.; Noé, P.; Bernard, M.; Fillot, F.; Bourgeois, G.; Garrione, J.; Perniola, L. Improved Electrical Performance Thanks to Sb and N Doping in Se-Rich GeSe-Based OTS Selector Devices. *2017 IEEE 9th Int. Mem. Work. IMW 2017* **2017**, 4–7.(1)

(39)   Clima, S.; Govoreanu, B.; Opsomer, K.; Velea, A.; Avasarala, N. S.; Devulder, W.; Shlyakhov, I.; Donadio, G. L.; Witters, T.; Kundu, S.; Goux, L.; Afanasiev, V.; Kar, G.S.; Pourtois, G. Atomistic Investigation of the Electronic Structure, Thermal Properties and Conduction Defects in Ge-Rich Ge_xSe_{1-x} Materials for Selector Applications. *Tech. Dig. - Int. Electron Devices Meet. IEDM* **2018**, 4.1.1-4.1.4.

4. Conclusion

In this dissertation, the GeTe/Sb$_2$Te$_3$ superlattice and the Ge$_x$Se$_{1-x}$ film utilizing ALD were developed. The successful deposition with high conformality could achieve a high-performance vertical-type CBA memory device which provides the most efficient way to stack memory layers for ultra-high density. The unique chemical affinity of ALD precursors to the SiO$_2$ and TiN surface and the two-dimensional nature of Sb$_2$Te$_3$ enabled to achieve an *in-situ* crystallized GeTe/Sb$_2$Te$_3$ superlattice film where the out-of-plane directions of the two-component layers precisely matched the c-axis. The GeTe/Sb$_2$Te$_3$ superlattice film showed ~1/7 RESET current of randomly oriented Ge$_2$Sb$_2$Te$_5$ alloy film due to the pressure-induced solid-state amorphization by the aligned superlattice. The reduction of RESET current with the aligned GeTe/Sb$_2$Te$_3$ superlattice films was also feasible in the vertical structure, showing the potentials of the current process for high-density and low-power V-CBA memory.

Deposition of Ge$_x$Se$_{1-x}$ films *via* ALD was performed for the envisioned application with selectors for the V-CBA memory combined with the ALD Ge-Sb-Te. Highly conformal Ge$_x$Se$_{1-x}$ films were obtained at low substrate temperatures ranging from 70 to 160 $^\circ$C. A unique deposition mechanism containing Ge intermediates provides a way to adjust the composition of the Ge-Se films from 5:5 to 7:3. Depending on the composition, low threshold

voltages ranging from 1.2 to 1.4 V were observed. Over 10^6 cycling endurance along with 10^4 half-bias nonlinearity was achieved with a $Ge_{0.6}Se_{0.4}$ composition, which is the highest among the reported OTS selectors deposited by ALD.

This thesis presents a new pathway for the next-generation phase-change memory by exploring the new ALD process of $GeTe/Sb_2Te_3$ superlattice and Ge_xSe_{1-x} films and suggesting the vertical-type CBA for futuristic memory with ultra-high density. Even though the phase-change memory is still far from the adoption as a universal memory, the results in this thesis could shed light on this field by suggesting new pathways different from the conventional approach.

Abstract (in Korean)

칼코제나이드 재료 기반 상변화 메모리 (PCM)의 광범위한 연구와 상용화에도 불구하고 Ge-Sb-Te 기반 PCM의 고밀도 및 저전력 메모리 개발은 아직 달성되지 못했다. 이는 주로 PCM에 사용되는 칼코제나이드 재료의 원자층 증착법 (ALD)과 같은 등각성 박막 성장 기술이 부족하기 때문이다. 현재 PCM의 아키텍처는 같은 평면상에 두 전극이 교차되는 크로스바 어레이 (CBA) 구조를 갖는다. CBA는 각 적층층에 필요한 리소그래피 공정 추가와 그에 필요한 마스크 제조 비용이 증가한다. 뿐만 아니라 전극 작동을 관장하는 주변부 또한 넓어져 현 시대가 필요로 하는 초고밀도 요구를 충족할 수 없다. 이는 이미 150단 이상의 레이어 스택으로 그 성능이 입증된 V-NAND 수직형 아키텍처로 해결할 수 있다. 수직형 아키텍처는 같은 면적 내에 많은 메모리를 제작할 수 있어 고밀도 메모리 개발에 적합하다. 하지만 고집적 수직형 크로스바 어레이 (V-CBA) 메모리 개발을 위해서는 Ge-Sb-Te 상변화 재료의 위상변화 층과 오보닉 쓰레스홀드 스위칭 (OTS) 선택소자 층을 수직 아키텍처의 에칭된 측벽에 균일하게 증착해야만 한다. 따라서 등각성 박막 성장 기술인 ALD 증착법이 필수적이다. 한편, Ge-Sb-Te 상변화 재료는 데이터를 저장시 요구되는 전력이 높다는 또 다른 심각한 단점을 갖고있다.

본 학위논문은 평면 및 수직 측벽 영역 모두에서 $GeTe/Sb_2Te_3$ 초격자 박막의 ALD 증착을 보여준다. SiO_2 및 TiN 표면에서 ALD 전구체들간의 독특한 화학적 반응과 Sb_2Te_3의 2차원적 특성으로 결정화된 초격자 필름을 증착할 수 있었다. $GeTe/Sb_2Te_3$ 초격자 박막은 기판에 특정 방향의 배향성을 갖고 성장시킬 수 있었으며 무작위로 배향된 $Ge_2Sb_2Te_5$ 박막

대비 1/7 가량 감소한 동작 전류를 나타냈다. 배향된 GeTe/Sb_2Te_3 초격자 필름 증착은 수직 아키텍처의 에칭된 측벽에도 적용 가능하여 동작 전류를 낮출 수 있었으며, 이는 GeTe/Sb_2Te_3 초격자의 V-CBA 메모리에 대한 잠재력을 보여준다.

ALD를 이용한 Ge_xSe_{1-x} 박막 증착 또한 ALD Ge-Sb-Te와 결합해 V-CBA 메모리의 선택소자에 적용되기 위해 연구됐다. 70 ~ 160 도의 낮은 기판온도에서 박막을 증착할 수 있었고 복잡한 구조에서도 균일하게 성장되는 Ge_xSe_{1-x} 박막을 얻을 수 있었다. Ge 중간전구체를 형성시키는 독특한 증착 메커니즘은 Ge-Se 필름의 조성을 5:5에서 7:3까지 조절할 수 있었고 각 조성에 따라 1.2 ~ 1.4 V의 낮은 문턱전압이 나타났다. 특히 $Ge_{0.6}Se_{0.4}$ 조성의 박막은 10^4의 비선형성으로 10^6번 이상의 높은 동작 내구성을 보였으며, 이는 ALD로 증착된 OTS 선택소자 중에서 가장 높은 수치이다.

주요어: 상변화 메모리, PCM, 크로스바 어레이, 수직 소자, 원자층 증착법, ALD, 칼코나이드, GeTe/Sb_2Te_3 초격자, $Ge_2Sb_2Te_5$, OTS, 선택소자, Ge_xSe_{1-x}

학 번: 2016 – 20804

유 찬 영